The Journal of Clinical Investigation

N-Myc-mediated epigenetic reprogramming drives lineage plasticity in advanced prostate cancer

Adeline Berger, … , Himisha Beltran, David S. Rickman

J Clin Invest. 2019. https://doi.org/10.1172/JCI127961.

Research In-Press Preview **Genetics** **Oncology**

Despite recent therapeutic advances, prostate cancer remains a leading cause of cancer-related death. A subset of castration resistant prostate cancers become androgen receptor (AR) signaling-independent and develop neuroendocrine prostate cancer (NEPC) features through lineage plasticity. These NEPC tumors, associated with aggressive disease and poor prognosis, are driven, in part, by aberrant expression of N-Myc, through mechanisms that remain unclear. Integrative analysis of the N-Myc transcriptome, cistrome and interactome using in vivo, in vitro and ex vivo models (including patient-derived organoids) identified a lineage switch towards a neural identity associated with epigenetic reprogramming. N-Myc and known AR-co-factors (e.g., FOXA1 and HOXB13) overlapped, independently of AR, at genomic loci implicated in neural lineage specification. Moreover, histone marks specifically associated with lineage-defining genes were reprogrammed by N-Myc. We also demonstrated that the N-Myc-induced molecular program accurately classifies our cohort of patients with advanced prostate cancer. Finally, we revealed the potential for EZH2 inhibition to reverse the N-Myc-induced suppression of epithelial lineage genes. Altogether, our data provide insights on how N-Myc regulates lineage plasticity and epigenetic reprogramming associated with lineage-specification. The N-Myc signature we defined could also help predict the evolution of prostate cancer and thus better guide the choice of future therapeutic strategies.

N-Myc-mediated epigenetic reprogramming drives lineage plasticity in advanced prostate cancer

Adeline Berger[1,10], Nicholas J. Brady[1,10], Rohan Bareja[2], Brian Robinson[1,2], Vincenza Conteduca[3], Michael A. Augello[4], Loredana Puca[3], Adnan Ahmed[5], Etienne Dardenne[1], Xiaodong Lu[6], Inah Hwang[1], Alyssa M. Bagadion[1], Andrea Sboner[1,2,7,8], Olivier Elemento[2,7,8], Jihye Paik[1,8], Jindan Yu[6], Christopher E. Barbieri[2,4,8], Noah Dephoure[5,8], Himisha Beltran[2,3,9] and David S. Rickman[1,2,8,*]

[1] Department of Pathology and Laboratory Medicine,
[2] Caryl and Israel Englander Institute for Precision Medicine, New York-Presbyterian Hospital,
[3] Department of Medicine,
[4] Department of Urology,
[5] Department of Biochemistry, Weill Cornell Medicine, New York, NY.
[6] Department of Medicine, Feinberg School of Medicine, Northwestern University, Chicago, IL.
[7] Department of Physiology and Biophysics, Institute for Computational Biomedicine,
[8] Meyer Cancer Center, Weill Cornell Medicine, New York, NY.
[9] Department of Medical Oncology, Dana Farber Cancer Institute, Boston, MA.
[10] Co-first authors

[*] Corresponding Author:
David S. Rickman
Weill Cornell Medicine
1300 York Avenue
New York, NY 10065
+1) 212-746-9171
dsr2005@med.cornell.edu

Conflict of Interest: The authors have declared that no conflict of interest exists.

Abstract

Despite recent therapeutic advances, prostate cancer remains a leading cause of cancer-related death. A subset of castration resistant prostate cancers become androgen receptor (AR) signaling-independent and develop neuroendocrine prostate cancer (NEPC) features through lineage plasticity. These NEPC tumors, associated with aggressive disease and poor prognosis, are driven, in part, by aberrant expression of N-Myc, through mechanisms that remain unclear. Integrative analysis of the N-Myc transcriptome, cistrome and interactome using in vivo, in vitro and ex vivo models (including patient-derived organoids) identified a lineage switch towards a neural identity associated with epigenetic reprogramming. N-Myc and known AR-co-factors (e.g. FOXA1 and HOXB13) overlapped, independently of AR, at genomic loci implicated in neural lineage specification. Moreover, histone marks specifically associated with lineage-defining genes were reprogrammed by N-Myc. We also demonstrated that the N-Myc-induced molecular program accurately classifies our cohort of patients with advanced prostate cancer. Finally, we revealed the potential for EZH2 inhibition to reverse the N-Myc-induced suppression of epithelial lineage genes. Altogether, our data provide insights on how N-Myc regulates lineage plasticity and epigenetic reprogramming associated with lineage-specification. The N-Myc signature we defined could also help predict the evolution of prostate cancer and thus better guide the choice of future therapeutic strategies.

Introduction

Lineage plasticity, a process by which differentiated cells lose their identity and acquire an alternative lineage program, has recently been identified as an emerging mechanism of resistance to targeted therapies in several cancer types, including prostate cancer (1-3). Under pressure of androgen receptor (AR)-directed therapies, a subset of patients with castration-resistant prostate cancer (CRPC) develop tumors that lose AR expression, AR-signaling dependence, luminal prostate cancer markers and acquire alternative lineage programs, including the development of small cell neuroendocrine carcinoma (neuroendocrine prostate cancer (NEPC) (1, 4, 5)). Few treatment options currently exist for patients developing NEPC and patient prognosis is poor. Although NEPC tumors arise clonally from prostate adenocarcinoma and share genomic alterations, there is significant epigenetic deregulation during the plasticity process (1). In the last decade, we and others have identified several candidate drivers of plasticity including, but not limited to, loss of TP53 and RB1 (6-12), loss of REST (13), and upregulation of MYCN (1, 14-17), EZH2 (7, 15), BRN2 (18), and SOX2 (7, 9, 18).

N-Myc (encoded by *MYCN*) is a transcription factor of the Myc family, essential for normal brain development during embryogenesis. Often amplified and overexpressed in neuroblastoma, medulloblastoma, retinoblastoma, astrocytomas, and glioblastoma multiforme (19-24), N-Myc has also been implicated in non-neuronal tumors, including prostate cancer, lymphomas, AML, rhabdomyosarcomas, Wilms tumors, small cell lung cancer and pancreatic tumors (25-33) (reviewed here (34)). N-Myc is not normally expressed in the prostate epithelial lineage but is overexpressed in the majority of NEPC and a subset of CRPC adenocarcinomas (CRPC-Adeno) (14, 15). N-Myc forms a heterodimer with Max and specifically binds DNA at E-box motifs to activate or repress gene expression depending on recruited co-factors (35). Genes involved in cell cycle, proliferation and apoptosis are the most well described targets of N-Myc across different cell types (36).

In this study, we describe a novel role for N-Myc in prostate cancer, characterized by changes in the N-Myc cistrome, its interacting co-factors, as well as reprogramming of the epigenome in an androgen-dependent manner. This reprogramming is associated with an induction of lineage plasticity in prostate cancer cells and a switch towards a neural identity that favors the development of AR independence and NEPC.

Results

Clinical NEPC is associated with neural lineage.

Although there is a spectrum within the pathologic subtype of NEPC, we have found that NEPC tumor cells defined by morphologic features often lose AR expression and express neuroendocrine markers (37). This observation suggests a transition from epithelial to neural lineage, which may involve dedifferentiation. To fully appreciate the spectrum of lineage states, we performed whole transcriptome analyses on patient samples, including the largest cohort of NEPC patients to-date. Gene expression was assessed from metastatic tumor biopsies of patients with pathology confirmed NEPC (n = 36) and CRPC-Adeno (n = 73), as well as from localized prostate adenocarcinoma (PCa) (n = 66). Relative to PCa, gene set enrichment analysis (GSEA) of our NEPC cohort data revealed a significant enrichment for stem cell genes associated not only with normal neuroendocrine cell precursors (neural crest stem cells (NCSC)), but also with activated neural stem cells (aNSC) (**Figure 1A, Table S1**). Unsupervised clustering analysis of the NEPC versus PCa leading-edge genes from embryonic stem cells (ESC), NCSC or NSC genesets (38-40) segregated patients according to their tumor histological classification (PCa, CRPC-Adeno or NEPC, **Figure S1A**). Interestingly, the stratification of CRPC-Adeno and NEPC patients based on levels of *MYCN* expression correlated with expression of neural lineage genes and inversely with AR signaling (**Figure 1A, Figure S1B**). To further validate the association with NSC genes, we purified murine NSC from the sub-ventricular zone and performed RNA-seq and histone-3 lysine-4 tri-methylation (H3K4me3) chromatin immunoprecipitation followed by DNA sequencing (ChIP-seq). From these studies, we combined the upregulated genes marked by H3K4me3 with publicly available single-cell RNA-seq data from activated NSC (41) and revealed a similar enrichment of NSC pathways in NEPC patient samples versus PCa samples (**Figure 1A**).

Moreover, we observed that high *MYCN* expression in patient CRPC-Adeno tumors was significantly associated with a worse overall survival compared to those with low *MYCN* expression (37.7 versus 80.3 months, hazard ratio (HR) = 1.95, 95% confidence interval (CI) 0.92-4.09, p-value = 0.04). This was also true for patients with NEPC (25.9 versus 41.4 months, HR = 3.31, 95% CI 1.22-9.09, p-value = 0.0064) as well as the combined cohort of all 81 patients (34.0 versus 76.5 months, HR = 2.27, 95% CI 1.24-4.11, p-value = 0.002, **Figure 1B**). While these data reveal that *MYCN* expression correlates with neural-lineage programs and poor clinical outcome, in both CRPC and NEPC patients, the underlying mechanism remains poorly described. We therefore sought to determine the precise mechanism that drives a prostate tumor epithelial cell to lose its luminal markers and gain a more neural-like lineage.

AR signaling alters the N-Myc transcriptome in vivo.

While N-Myc cooperates with enhancer of zeste homolog 2 (EZH2) to abrogate AR signaling (15), the role of N-Myc in driving lineage plasticity in an NEPC-like context of low to no AR signaling has not been characterized. Using our previously described *Pb-Cre*$^{+/-}$*; Pten*$^{f/f}$*; LSL-MYCN*$^{+/+}$ genetically engineered mouse model (GEM) which overexpresses human *MYCN* (15), we found that N-Myc overexpression led to the formation of prostate tumors with 100% penetrance compared to *Pb-Cre*$^{+/-}$; *Pten*$^{f/f}$; *LSL-MYCN*$^{-/-}$ mice (**Figure S2A**). Interestingly, survival of *Pb-Cre*$^{+/-}$*; Pten*$^{f/f}$*; LSL-MYCN*$^{+/+}$ mice was increased by an average of 12 weeks in response to castration (**Figure S2A**). This is likely due to the fact that the tumors are heterogeneous with a component of AR-responsive adenocarcinoma, consistent with data from another GEM model of adenocarcinoma to NEPC transformation (7). Despite the prolonged survival, castrated mice developed invasive prostate tumors that metastasized to multiple locations, including the liver, at 6 months post-castration. We also noted an increase in poorly differentiated foci that lost expression of luminal (AR, cytokeratin 8 (KRT8)) and basal (KRT5) markers and gained expression of the epithelial-mesenchymal transition marker vimentin (VIM) and the NEPC marker neural cell adhesion molecule (NCAM1 (37, 42), **Figure 2A**). Primary and metastatic lesions in castrated mice contained tumor foci with up to 90% of the total tumor area comprised of divergent differentiation (e.g., intestinal, squamous, sarcomatoid as previously described (15) or chondroid differentiation) compared to up to 25% in the intact animals (**Figure S2B,C**). In addition, we observed large foci of neural differentiation characterized by ganglion-like cells. These cells had abundant eosinophilic cytoplasm and nuclei with prominent, centrally located nucleoli. Immunohistochemical staining of serial 4 µm tissue sections revealed populations of cells that were either positive for epithelial (AR and KRT8), mesenchymal (VIM) or neural markers (S100) but also contained cells that were positive for multiple lineages (AR and VIM) (**Figure S2D**). This suggests that these double positive cells may be transitioning from one lineage to another, similar to what has been observed in other mouse models (7, 12, 16). The ganglion differentiation is also consistent with previous observations made in N-Myc-driven neuroblastoma models (43). The loss of AR and gain of VIM and S100 suggest further differentiation towards the neural lineage, and some of the VIM/S100-positive cells have invaded the local vasculature (**Figure 2B**), consistent with a pro-metastatic phenotype. These data suggest that the removal of androgen signaling enables a wider variety of N-Myc-induced differentiation programs.

To further define the transcriptional differences regulated by N-Myc in an androgen-dependent manner, we performed RNA-seq on N-Myc-expressing 22Rv1 xenografts grown in castrated or intact recipients. Transcriptome-wide analyses revealed that castration was associated with a significant increase in the number of N-Myc-deregulated target genes (**Figure 2C)**. In castrated 22Rv1 xenograft mice, the N-Myc-signature was enriched with genes associated with neural lineage pathways (**Figure 2C**), including neural progenitor cells (NPC) bivalent genes (H3K4me2/3 active and H3K27me3 repressive marks (44, 45), NES = 2.00, FDR q-value = 0.004), in addition to genes implicated in neural development (e.g. *SOX11, SOX21, NTRK1, NKX2-1*), expressed in adult stem cells (e.g. *HOXA2/A3/A9/A10* and *WNT5A*), ES cells (e.g. *SOX2*) or NEPC (e.g. *CHGA*), while epithelial–lineage associated genes were downregulated (**Figure 2C**). Similar observations were made in the GEM model (**Figure S2E**). Importantly, both 22Rv1-CTL and 22Rv1-N-Myc cells express the AR variant ARv7 (**Figure S3A/B**). Despite ARv7 expression, androgen response genesets were significantly downregulated in response to castration, as observed by GSEA (**Figure S3C**), and N-Myc expression blocked the upregulation of ARv7 target genes (46) after castration (**Figure S3D**). These data suggest that the removal of circulating androgen and AR signaling may impact N-Myc gene regulation. Since these datasets were generated from tumors following chronic androgen deprivation, we cannot rule out that these molecular changes did not evolve over time.

N-Myc expression leads to neural lineage gene expression and reduced androgen response.

To directly assess the impact of acute removal of androgen on the N-Myc-induced molecular program, we performed, in replicate, RNA-seq in isogenic LNCaP cells (+/- *MYCN* (15)) following short-term androgen withdrawal. LNCaP cells, a hormone-naive prostate cancer cell line with a well-characterized luminal/epithelial phenotype, were starved in androgen-deprived media for 72 hours, and subsequently re-exposed to androgen or maintained in androgen-deprived conditions for an additional 24 hours (**Figure 3A**). RNA-seq data revealed a distinct N-Myc driven transcriptional program with 8,585 genes differentially regulated in N-Myc cells compared to control (CTL) cells (**Figure S4A**). Consistent with our observations in vivo, androgen withdrawal significantly altered the N-Myc signature in vitro (13% and 42% of the N-Myc target genes are differentially regulated specifically in the presence or absence of androgen, respectively, **Figure S4A**). While, in the presence of androgen, AR signaling was enriched in LNCaP-CTL cells compared to N-Myc cells as expected (15) (**Figure 3B**), N-Myc-upregulated genes were enriched with stem cell signatures and markers of neural lineage differentiation in the absence of androgen (**Figure 3B**). These changes were shown to be N-Myc-dependent, as shRNA-mediated knockdown of N-Myc reversed their expression (e.g. *AUTS2* and *NKX2-1*, **Figure S4B**). To determine if the transcriptional changes were stable, we maintained cells in androgen-deprived condition for 41 days followed by a 24-hour androgen stimulation (**Figure 3A**). After long-term withdrawal, the response of AR-target genes to androgen stimulation was dramatically reduced (over 80% for *KLK4*, **Figure 3C**). Moreover, expression of genes associated with the neural lineage were increased significantly in LNCaP-N-Myc cells (**Figure 3C,D, Figure S4C,D**) and N-Myc expression led to increased enrichment at day 42 compared to day 4 for neural lineage and stem cell genesets, including an adult stem cell signature associated with small cell neuroendocrine cancers from multiple epithelial tissues (47). N-Myc expression was also associated with reduced global responsiveness to androgen re-stimulation, with fewer genes being differentially expressed at day 42 in LNCaP-N-Myc cells compared to LNCaP-CTL cells (**Figure 3E**). Altogether, these data support the hypothesis that there is interplay between AR and N-Myc signaling that propagates lineage plasticity.

The N-Myc cistrome is distinct from C-Myc and altered by AR signaling.

As a transcription factor, N-Myc regulates gene expression by binding to DNA and modulating transcriptional activity. To fully describe the genomic loci where N-Myc is bound, we performed N-Myc ChIP-seq in LNCaP-N-Myc cells or isogenic LNCaP-CTL cells following acute androgen withdrawal (**Figure 3A**). We observed N-Myc binding as a narrow peak mainly within

2 kilobases (Kb) of gene transcription start sites (TSS, **Figure 4A**) irrespective of androgen. Approximately 40%, 25% and 25% of N-Myc peaks were within intronic, intergenic and promoter/TSS regions, respectively. To define N-Myc-specific binding in prostate cancer cells, we compared the N-Myc cistrome (LNCaP-N-Myc cells with androgen) with the C-Myc cistrome (LNCaP cells with androgen) and with publicly available N-Myc ChIP-seq data from a *MYCN*-amplified neuroblastoma model (48). Approximately half of the N-Myc bound sites were shared with C-Myc in LNCaP cells and/or N-Myc in neuroblastoma cells (**Figure 4B,C**). The genes uniquely bound by C-Myc in LNCaP cells were enriched with cell cycle and cell proliferation-related genes, corresponding to the most well characterized functions of Myc family proteins (36), while the genes uniquely bound by N-Myc in neuroblastoma cells were neural lineage-related. Despite these overlaps, we observed that 44% of the N-Myc bound sites are specific to the prostate cancer cells and that these prostate-specific N-Myc-bound genes are enriched for neural-lineage genes (**Figure 4D**). Moreover, while the C-Myc-specific and N-Myc/C-Myc-shared bound sites were enriched for E-box motifs, the N-Myc-specific sites in LNCaP cells were significantly enriched for Forkhead motifs (**Figure S5A**). The difference between N-Myc and C-Myc binding in prostate cancer cells is also in accordance with the different profiles of expression of *MYC* and *MYCN* mRNA in prostate adenocarcinoma (high *MYC*, low *MYCN*) versus NEPC (low *MYC*, high *MYCN*, **Figure S5B**). Intriguingly, N-Myc binds near the TSS of the *MYC* locus and may help to enforce the selective pattern of N-Myc/C-Myc expression (**Figure S5C**). Together these results suggest that, while Myc-family members share a number of common targets, they are not completely functionally-redundant and have specific targets, that are regulated in a cell type-dependent manner.

To determine if the androgen-dependent changes in gene regulation were explained by a change in N-Myc binding to chromatin, we compared the binding profiles obtained in the two conditions. We found that 42% of N-Myc binding was dynamic, changing in different contexts of AR signaling (**Figure 4E**). Upon androgen withdrawal, N-Myc binding was depleted or reduced from 36% of total bound sites, while enriched or newly bound to 6% (**Figure 4E, Figure S5D**). These dynamic N-Myc peaks were less enriched at promoter/TSS regions and more enriched at intergenic and intronic regions (**Figure 4E)**. The distribution of dynamic N-Myc binding was confirmed by performing ChIP-seq in N-Myc-expressing 22Rv1 xenografts from castrated or intact recipients (**Figure 4E**). We also found that the peaks shared with and without androgen were closer to TSS than the peaks specific to one condition (**Figure S5E**) and were enriched at genes involved in normal cellular homeostasis (**Figure S5F**).

N-Myc interacts with known AR co-factors to alter DNA binding.

Differential interactions between N-Myc and transcriptional co-factors or pioneering factors could explain the observed dynamic binding genome-wide. It has been shown that less than half of Myc binding sites on chromatin have consensus E-box motifs and many do not even show variant E-boxes (49, 50), concluding that the E-box enhances chromatin association but is not a prerequisite for binding. Most likely, therefore, protein/protein interactions play a large role in targeting N-Myc to sites on chromatin. To reveal such co-factors, we performed a de novo motif discovery in 200 bp regions surrounding all N-Myc binding sites identified by ChIP-seq. Motif analysis of the unique and enriched N-Myc peaks revealed that, in addition to E-boxes, there was a significant enrichment of motifs consistent with forkhead box (FOX) and homeobox (HOX) family members (**Figure 5A, Figure S6A**). Since FOXA1 and HOXB13 are critical AR-coregulators (51-55), we performed HOXB13 and FOXA1 ChIP-seq in the LNCaP-N-Myc cells.

Unlike for HOXB13, we found that androgen withdrawal dramatically altered the FOXA1 cistrome (31% unique peaks, **Figure 5B**). With respect to the unique N-Myc peaks in the absence of androgen, there was very little overlap (< 20%) with the C-Myc, N-Myc in neuroblastoma or AR cistromes, compared to the N-Myc common peaks (**Figure 5C**). In contrast, N-Myc unique peaks without androgen shared more binding sites with AR co-factor cistromes defined in the presence of androgen in N-Myc cells versus CTL cells (from 39% to 51% for FOXA1 and from 12% to 29% for HOXB13). This overlap was further increased for FOXA1 following androgen withdrawal (+10%, **Figure 5C**). Taken all together, 57% of all enriched and unique N-Myc peaks without androgen were co-bound with AR, HOXB13 or FOXA1 either alone or in combination (**Figure 5D**). In agreement with the motif analysis, comparison of the genomic loci bound by N-Myc after androgen withdrawal revealed nearby binding of FOXA1 and/or HOXB13 (**Figure 5E).** Furthermore, while epithelial lineage genes were enriched at these co-bound sites as expected, there was also a significant enrichment of neural lineage genesets (**Figure S6B**). To directly assess the ability of a prostate lineage-defining factor, such as FOXA1, to modulate N-Myc binding at neural lineage genes, we performed siRNA-mediated knockdown of FOXA1 and performed N-Myc ChIP-qPCR at binding sites identified by ChIP-seq (**Figure 5F**). Despite a knockdown of only 50%, we observed a significant decrease in N-Myc binding on the target neural genes *NKX2-1* and *CHGA*, suggesting a role for FOXA1 in regulating N-Myc binding (**Figure 5F**).

To identify other proteins that could regulate N-Myc binding, we performed Rapid Immunoprecipitation Mass Spectrometry of Endogenous Proteins (RIME) (56) in LNCaP-N-Myc cells. While a subset of common interactors demonstrated increased affinity between the conditions, no interactions specific to one condition versus another were observed (**Figure 5G**). The majority of interactions were shared between conditions and included well-known N-Myc interacting proteins (e.g. MAX and TRRAP (57-59)), proteins associated with heterochromatin (e.g. chromobox homologs (CBX) 1, 3 and 5) as well as HOXB13 (**Table S2**, **Figure 5G**). These data suggest that, while the ability to physically interact with N-Myc is not dramatically affected by the presence or acute withdrawal of androgen, N-Myc co-factors may direct genomic binding to sites in chromatin that are accessible specifically in one condition either through competition at N-Myc binding sites or by altering the chromatin accessibility.

N-Myc promotes bivalency on neural lineage genes.

On a global scale, gene transcription is also regulated by epigenetic modifications of histone proteins. Two of the major histone marks used to study the regulation of gene expression are H3K4me3 (associated with transcriptional activation) and H3K27me3 (associated with repression). Paradoxically, some genomic loci contain both marks (i.e. bivalent). Bivalently marked genes are typically transcriptionally poised, have been well characterized in ES cells and shown to be essential for development and lineage-determination (60, 61). The bivalent mark changes during the differentiation of the cells, through the action of histone modifiers, and biases gene expression towards activation (H3K4me3 only) or repression (H3K27me3 only) depending on the identity of each cell. To interrogate a putative role of N-Myc in regulating bivalency, we assessed the overlap between H3K4me3 and H3K27me3 ChIP-seq profiles, following short-term or long-term androgen withdrawal (**Figure 3A**). Interestingly, the distribution and density of H3K27me3 histone marks near H3K4me3 marks varied dramatically depending on N-Myc expression and androgen stimulation. While the H3K27me3 binding profile was narrow and centered on H3K4me3 peaks in LNCaP-CTL cells, the binding was redirected within a 3 Kb range around the H3K4me3 peaks in LNCaP-N-Myc cells yielding a multimodal distribution (**Figure 6A**). We also observed similar numbers of genomic loci marked by H3K4me3 alone, while only

N-Myc-overexpressing cells showed a significant increase in H3K27me3 (8.6-fold) and bivalent peaks (18-fold, **Figure 6B**) after androgen withdrawal. Bivalent genes in N-Myc cells were enriched for Polycomb Repressor Complex 2 (PRC2), neurogenesis and neural lineage pathways while bivalent genes in control cells were associated with gene regulation and stress response (**Figure 6B).** Integrating the RNA-seq data with H3K4me3/H3K27me3 ChIP-seq data revealed, as expected, low levels of gene expression associated with bivalent histone marks (**Figure S7A**). Interestingly, we found an increase of nearly 2-fold in the number of N-Myc peaks that are bivalent in absence versus presence of androgen, corresponding to 966 and 580 genes respectively (**Figure 6C, Table S3**). Moreover, androgen withdrawal dramatically increased the level of enrichment of PRC2 and neural-associated genes (**Figure S7B**). Among the N-Myc-bound, bivalent genes, a subset showed a decrease of H3K4me3 and an increase of H3K27me3 levels in the absence of androgen. An example of this was observed for the desmocollin 3 gene (*DSC3)*, which has been implicated in epithelial cell junctions (62). Inversely, genes such as *NKX2-1, SOX2, SOX11* and *SOX21*, became bivalent by gaining H3K4me3 marks in the N-Myc cells, suggesting the activation of gene expression (**Figure 6D, Figure S7C**). Binding at these regulated loci appeared to be specific for N-Myc in LNCaP cells compared to C-Myc in LNCaP and/or N-Myc in neuroblastoma (**Figure S7D**). Similar results were obtained by performing N-Myc/H3K4me3/H3K27me3 ChIP-seq in a NEPC patient-derived organoid (PM154, **Figure 6D, Figure S7C**). We thus hypothesized that the bivalent genes linked to neuronal identity would maintain H3K4me3 and be up-regulated following chronic androgen withdrawal, while the genes associated with an epithelial lineage would maintain H3K27me3 and become down-regulated over time. To assess this, we analyzed the expression levels of the 966 bivalently-marked, N-Myc-bound genes by RNA-seq following acute or chronic androgen withdrawal. Genes that were identified as bivalently-marked and N-Myc-bound at day 4, were enriched in LNCaP-N-Myc versus LNCaP-CTL cells, at day 42 (**Figure 6E**). Unsupervised clustering of the differentially expressed genes in LNCaP N-Myc versus LNCaP-CTL cells at day 42 revealed distinct transcriptional modules (**Figure 6F**). Cluster 1 included repressed epithelial-related or AR target genes (*ZBTB7A, ALDH1A3*), consistent with an increase of the repressive mark H3K27me3 on AR target genes (**Figure S4D**) and with previous findings (15). Conversely, Cluster 4 contained many of the neural lineage genes, which are upregulated by N-Myc following long-term androgen withdrawal (**Figure 6F**). Furthermore, we confirmed that 57% of the 966 bivalently-marked, N-Myc-bound genes at day 4 became marked only with H3K4me3 at day 42, with 30% remaining bivalently marked (**Figure S8A,B**), and the genes which became H3K4me3 marked only were significantly enriched for neural lineage genesets (**Figure S8C**).

To determine the clinical relevance of these findings, we queried the RNA-seq from our patient cohort and found that the 966 bivalent genes identified in androgen-deprived LNCaP-N-Myc cells successfully classified the PCa, CRPC-Adeno and NEPC patient samples into groups based on NEPC score (**Figure 7A, Figure S9A**) and were enriched in the NEPC samples (**Figure 7B**). The NEPC clinical samples were enriched for neural lineage-associated bivalent genesets compared to PCa or benign samples (**Table S4**). These findings also correlated with N-Myc expression level in both NEPC and CRPC-Adeno samples (**Figure 7B**). We observed a stepwise upregulation of the N-Myc-bound and bivalent neural-associated genes during the progression from PCa to NEPC, with upregulation of genes such as *SOX11* and *NKX2-1* and a corresponding downregulation of epithelial lineage-linked genes such as *FGFRL1* and *DSC3* (**Figure 7C, Figure S9B**). This suggests that these genes associated with bivalent marks in N-Myc-expressing cells play a critical role in prostate cancer evolution and may help to identify patients who are most likely to develop NEPC. Lastly, we performed N-Myc ChIP-seq in the patient-derived NEPC organoid PM154 and found that, despite fewer numbers of total peaks, 79% of the peaks were in common with LNCaP-N-Myc and 22Rv1-N-Myc xenografts, including neural lineage-associated genes (*NREP, ULK2, RAB39A*), bivalent genes (*RAB39A*), and the H3K27me3 writer *EZH2* (**Figure S9C,D**). Moreover, we confirmed the N-Myc-dependent upregulation of these bivalent genes in 22Rv1 xenografts and NEPC patient-derived organoid models (**Figure S9E**).

We have previously shown that, in the context of active AR signaling, N-Myc cooperates with EZH2 and redirects its activity to downregulate AR target genes (15). Using an *in situ* proximity ligation assay (PLA) to monitor EZH2 and N-Myc complex formation, we confirmed the presence of the EZH2/N-Myc complexes in LNCaP and 22Rv1-N-Myc cells with and without an active AR-signaling and in an AR-negative, NEPC patient-derived organoid (PM154, **Figure S9F**). This suggests that N-Myc and EZH2 maintain a protein-protein interaction in the absence of AR that may regulate the H3K27me3 status of the bivalent genes. To address this, we performed shRNA-mediated knockdown of EZH2 in PM154 cells. After validation on genes that have been previously shown to be regulated by EZH2, we observed that knockdown of EZH2 led to a dramatic upregulation of the bivalent genes that were previously downregulated by N-Myc and inversely (**Figure 7D**). In addition to shRNA strategies, PM154 cells were also treated with a pharmacologic EZH2 inhibitor (GSK503). Targeted GSEA demonstrated a significant de-enrichment of multiple neural lineage-associated bivalent genesets (**Figure 7B, Figure S9G**).

Discussion

Despite recent advances in the development of highly effective AR-directed therapies for the treatment of prostate cancer, acquired resistance ultimately ensues. Since AR-indifferent prostate cancer is thought to arise and evolve in the face of hormonal therapy, there is concern that the development of more potent AR-targeted treatments will increase the incidence of this lethal form of prostate cancer. Lineage plasticity as a mechanism of resistance to targeted therapies has been implicated in both epithelial tumors and leukemias, suggesting that significant findings may successfully translate to additional tumor types (1, 3, 7, 9, 12, 63-65). A recently published study using a machine-learning approach has identified a link between stemness and what is termed oncogenic dedifferentiation (66).

Here, we present data that highlights how an oncogenic transcription factor, N-Myc, can promote the acquisition of alternative lineage identities, including stem-like precursor states of the neural lineage, and explains the progression of dedifferentiation steps required during disease progression. We show that N-Myc functions in the epigenomic and transcriptomic reprogramming of prostate cancer epithelial cells in an androgen-dependent manner. Data from in vivo models revealed that N-Myc driven prostate tumors are more aggressive following castration, including the development of metastatic lesions and the aberrant acquisition of alternative lineage programs. Whether or not these changes involve a transient, undifferentiated stem-like state (7, 9, 47) or a direct transdifferentiation (12) and the role of the local microenvironment in dictating the choice of lineage remains to be elucidated.

The N-Myc-induced transcriptomic landscape also changed dramatically in vivo following castration. Integrative ChIP-seq/RNA-seq data revealed a rapid, androgen-dependent change in the N-Myc cistrome, transcriptome, and histone methylation. In the presence of androgen, N-Myc binds to regulatory sequences associated with AR binding, upstream of AR target genes, to suppress gene expression. Consistent with the overlap between AR and N-Myc binding, forkhead box and homeobox consensus motifs were significantly enriched in chromatin regions directly bound by N-Myc. Moreover, FOXA1 binding was associated with androgen-dependent changes in the N-Myc binding at genes associated with the neural lineage and was essential for N-Myc binding at the loci tested, including *NKX2-1* which has been implicated in neuroendocrine-like small cell lung cancers (67). Proteomic data confirmed an interaction between chromatin-bound N-Myc and the AR co-factor HOXB13, as well as identified interactions with the heterochromatin-associated proteins CBX1/3/5. Recent studies have implicated CBX3 in neural lineage specification, which could cooperate with N-Myc to facilitate lineage plasticity (68). In the absence of androgen, the N-Myc cistrome is re-directed towards promoters of genes expressed in neural precursors/NSC and is associated with transcriptional activation and reprogramming of epigenetic H3K4me3/H3K27me3 bivalent marks at neural lineage-associated genes. Finally, using proteomic approaches, we identified a number of previously uncharacterized N-Myc-interacting proteins that will provide potential targets to inform future studies of Myc-driven cancers.

Another important finding from this study came from our direct cistromic comparison of N-Myc and its related family member C-Myc in prostate cancer or N-Myc in neuroblastoma. The C-Myc locus is commonly amplified in early prostate cancer development (69) and we show that its expression decreases during disease progression. This may be partially explained by the deposition of H3K27me3 marks in the gene body following long-term androgen withdrawal (**Figure S5C**). Interestingly, a recent report suggested that, in a specific genetic context (Rb1/Trp53 loss; AKT; BCL2 induction), C-Myc expression in prostate basal cells leads to the development of NEPC (67). We found that in LNCaP cells (*RB1* and *TP53* wild type), 49% of N-Myc binding does not overlap with C-Myc binding. We also found that these N-Myc-specific sites are enriched for genes associated with the neural lineage. Altogether, this suggests that N-Myc and C-Myc share common functions but N-Myc may also regulate molecular programs that are not driven by C-Myc in prostate cancer cells. This is consistent with other data from prostate cancer (69-72) as well as several other solid tumors, such as lung (73-79) and pancreas (26, 80, 81).

Our studies have identified a potential mechanism by which N-Myc overexpression and its subsequent DNA binding induce epigenomic and transcriptomic reprogramming resulting in a castration-resistant, lineage plastic phenotype that gives rise to NEPC. These data provide new insights into the early events of lineage switching as a mechanism of escape to the effects of hormone therapy in prostate cancer. More intriguingly, the changes that occur in the face of AR targeted therapy may also provide a molecular signature to classify prostate cancer patients and potentially help predict those approximately 20% of CRPC patients that may eventually develop NEPC (82, 83). Clinical trials have been developed for patients with NEPC, targeting Aurora Kinase, Notch and PD-1 pathways (NCT01799278, NCT02709889, NCT03179410). Additionally, EZH2 inhibitors have entered early stage clinical trials in patients with a wide range of tumor types (NCT03525795, NCT02860286), including prostate (NCT03480646). Identifying the patients most at-risk of developing NEPC could provide opportunities for earlier clinical intervention and allow for inclusion in future clinical trials of these novel targeted therapies in NEPC.

Methods

Cell Culture

Human LNCaP and 22Rv1 male prostate cancer cells lines were obtained from ATCC and maintained as recommended. LNCaP cells overexpressing N-Myc or an empty vector control were cultured in RPMI 1640 medium (Gibco, 11875-093) supplemented with 10% FBS (Gemini, 900-108) and 1% penicillin/streptomycin (Gibco, 15140-122). For androgen-deprivation treatment, the cells were cultured in phenol-red free RPMI medium (Gibco, 11835-030) supplemented with 5% charcoal stripped serum (Gibco, A33821-01) and 1% penicillin/streptomycin. The medium was then supplemented with 10 nM of DHT (Sigma-Aldrich, D-073) or the equivalent volume of ethanol for 24 hours. LNCaP cells maintained more than 7 days in androgen-deprived media detached from the flask and were then kept in culture as cells in suspension. PM154 and PM155 cells were cultured as previously described (84). PM154 were treated with GSK503 (5µM) or vehicle for 6 days before RNA collection used for RNA-seq. CD133$^+$/EGFR$^+$ NSC were isolated from the subventricular zone of P1 neonatal mouse brain and cultured in N2 media with 20 ng/mL EGF (PeproTech, AF-100-15) and bFGF (PeproTech, 100-18B).

Immunoblot Analysis

Protein lysates were collected in RIPA buffer (Thermo Scientific, 89901) supplemented with protease inhibitor cocktail and phosphatase inhibitors (Thermo Scientific, 78428/78430). Each protein sample was resolved by SDS–PAGE (Bio-Rad, 4561084), transferred onto a PVDF membrane (Thermo Scientific, IB24002) and incubated overnight at 4°C with primary antibodies: N-Myc (Santa Cruz, sc-53993), FOXA1 (Abcam, ab23738), EZH2 (Active Motif, 39901), AR (Millipore, 06-680), ARv7 (RevMab, 31-1109-00), GAPDH (Millipore, AB2302). The membrane was then incubated for 1 hour at room temperature with horseradish peroxidase-conjugated secondary antibody (Cell Signaling, 7074/7076; Abcam, ab97135) and immune complexes were visualized by enhanced chemiluminescence detection (Millipore, WBLUF0500).

Quantitative PCR

RNA extraction was performed using the NucleoSpin RNA Plus extraction kit (Macherey-Nagel, 740984) following the manufacturer's recommendation. qRT-PCR was performed using Power SYBR Green Kit (Applied Biosystems, 4389986) following the manufacturer's recommendation and data were acquired with the QuantStudio 5 Real-Time PCR System (Applied Biosystems). Primer sequences can be found in **Table S5**.

Clinical Analysis and RNA Extraction from Prostate Cancer Samples

Patients were enrolled on an IRB approved protocol with informed consent and data were analyzed as previously described (1, 85). For these studies, 81 patients (57 metastatic castrate-resistant prostate adenocarcinoma (CRPC-Adeno), 24 metastatic neuroendocrine prostate cancer (NEPC)) with outcomes data were analyzed for overall survival. Patients were divided into two categories according to the median value of *MYCN* expression. Univariate overall survival analysis was calculated from the time of initial diagnosis of metastatic disease to death from any cause. Patients still alive at time of last follow-up were censored. For transcriptomic analysis, 29 benign prostate tissues, 66 localized prostate cancer (PCa), 73 metastatic CRPC-Adeno, and 36 metastatic NEPC were selected for further analysis. Tumor histology was confirmed in all cases by pathology review and morphologic classification (37). RNA was extracted from frozen material for RNA-seq using the Maxwell 16 LEV simplyRNA Tissue Kit (Promega, AS1280). Specimens were prepared for RNA sequencing as previously described (86). RNA integrity was verified using the Agilent Bioanalyzer 2100 (Agilent Technologies). Paired-end sequencing was performed on Illumina GAII, HiSeq 2000, or HiSeq 2500 instruments.

RNA-seq Analysis

Quality control of raw sequencing reads was performed using FastQC (Babraham Bioinformatics). Low-quality reads were removed using Trimmomatic (87) with a sliding window size of 4bp and a quality threshold of 20. The resulting reads were aligned to GRCm38 or GRCh38 using STAR (88). Reads were sorted and indexed using SAMtools (89). Transcript abundance was calculated in FPKM using Cufflinks (90) and in gene counts using HTSeq (91). Differential gene expression was assessed using DESeq2 (92). Batch normalization of patient samples was done using ComBat (93) from the sva Bioconductor package(94). Rstudio (1.0.136) with R (v3.3.2) and ggplot2 (2.2.1) were used for the statistical analysis and the generation of figures depicting the expression levels in each of the classes.

Chromatin Immunoprecipitation

Cells were collected with trypsin (Gibco, 25300-120) and crosslinked in media containing 1% methanol-free formaldehyde (Thermo Scientific, 28908) and quenched for 8 min using 125 mM glycine. The cell pellets were centrifuged and washed twice in cold PBS. Each pellet was resuspended in 1 milliliter of lysis buffer (50 mM Tris HCl pH 8, 0.5% SDS, 10 mM EDTA with protease and phosphatase inhibitors (Thermo Scientific, 78428/78430)) and lysed for 20 minutes at 4°C. The nuclei were collected by centrifugation and resuspended in a second lysis buffer (10 mM Tris HCl pH 7.5, 150 mM NaCl, 0.1% SDS, 1 mM EDTA, 1% NP-40, 1% sodium deoxycholate, with protease and phosphatase inhibitors (Thermo Scientific, 78428/78430)). The protein-bound chromatin was sheared by sonication (Diagenode, Bioruptor Pico). Equal volumes of sheared chromatin were immunoprecipitated with N-Myc antibody (Santa Cruz, sc-53993), C-Myc (Santa Cruz, sc-764), H3K4me3 (Millipore, 17-678), H3K27me3 (Abcam, ab6002), FOXA1 (Abcam, ab23738), HOXB13 (Cell Signaling, 90944), or IgG control (Santa Cruz, sc-2025).

Following extensive washing, the immunoprecipitated sheared chromatin was eluted in a fresh buffer containing 100 mM $NaHCO_3$ and 1% SDS. The reverse crosslinking was performed with 45 mM Tris pH 7, 170 mM NaCl at 65°C overnight. After RNAse and proteinase K treatment, the DNA fragments were purified using the NucleoSpin Gel and PCR Clean-up Kit (Macherey-Nagel, 740609) following the manufacturer's recommendation. The libraries were generated using the Hyper Prep Kit (Kapa Biosystems, KK8502) and were assessed for quality, purity, and size using DNA High Sensitivity Bioanalyzer chips (Agilent, 5067-4626). Those passing QC were quantified using the Illumina Library Quantification Kit (Kapa Biosystems, KK4854). The sequencing was performed by the Weill Cornell Medicine Genomics and Epigenomics Core using Illumina HiSeq 2500 or 4000 instruments.

Public ChIP-seq Data

Publicly-available ChIP-seq data were obtained from the Gene Expression Omnibus using the following accession numbers: AR and FOXA1 from parental LNCaP cells (GSE69045), and N-Myc from BE2C neuroblastoma cells (GSE80151).

ChIP-seq Analysis

Quality control of raw sequencing reads was performed using FastQC (Babraham Bioinformatics). Low-quality reads were removed using Trimmomatic (87) with a sliding window size of 4bp and a quality threshold of 20. The resulting reads were aligned to GRCh38 using Bowtie2 (95). PCR duplicates introduced during library creation were removed using SAMtools (89). ChIP-seq peaks were called using MACS2 (96) with default parameters and q-value threshold (0.05 for C-Myc ChIP-seq in LNCaP cells and N-Myc ChIP-seq in 22Rv1 xenografts and PM154 organoid; 0.01 for N-Myc ChIP-seq in BE2C cells and for H3K4me3, FOXA1, AR or HOXB13 ChIP-seq in LNCaP cells; 0.0001 for N-Myc ChIP-seq in LNCaP cells), or with the broad-peak option enabled and a broad-cutoff q-value threshold (0.1 for H3K27me3 ChIP-seq in LNCaP cells). Sequencing reads from sonicated input chromatin derived from each individual cell line in each condition was used as a control for peak calling.

Downstream Analysis of Sequencing Data

Enriched ChIP-seq peak regions were annotated to hg38 genomic features and assessed for the presence of transcription factor motifs +/- 100bp from the ChIP-seq peak using HOMER (97). Regions of ChIP-seq overlap were defined using BEDTools (98). ChIP-seq enrichment profile plots and heatmaps were generated using deepTools (99). Gene set enrichment analysis (GSEA) (39) was performed using gene sets included in the Molecular Signature Database.

RIME

RIME was performed as previously described (56) with modifications. Briefly, cells were collected with trypsin (Gibco, 25300-120) and crosslinked in media containing 1% methanol-free formaldehyde (Thermo Scientific, 28908) for 10 minutes at room temperature and quenched for 8 min using 125 mM glycine. The cell pellets were centrifuged and washed twice in cold PBS. Each pellet was resuspended in 1 milliliter of lysis buffer (50 mM Tris HCl pH 8, 0.5% SDS, 10 mM EDTA with protease and phosphatase inhibitors (Thermo Scientific, 78428/78430) and lysed for 20 minutes at 4°C. The nuclei were collected by centrifugation and resuspended in a second lysis buffer (10 mM Tris HCl pH 7.5, 150 mM NaCl, 0.1% SDS, 1 mM EDTA, 1% NP-40, 1% sodium deoxycholate, with protease and phosphatase inhibitors (Thermo Scientific, 78428/78430)). The protein-bound chromatin was sheared by sonication for 10 minutes (Diagenode, Bioruptor Pico). Equal volumes of sheared chromatin were immunoprecipitated overnight with N-Myc antibody (Santa Cruz, sc-53993) or mouse IgG (Santa Cruz, sc-2025) bound to Protein G magnetic beads (Invitrogen, 10004D). Beads were washed 10 times in RIPA buffer and 2 times in 100 mM ammonium bicarbonate (AMBIC) solution (Alfa Aesar, A18566). On-bead enzymatic digestion was performed overnight at 37°C with 100 ng trypsin (Worthington Biochemicals, LS003740). An additional 100 ng was added for 4 hours prior to desalting.

Peptides were desalted on hand-packed C18 STAGE tip columns (100). Eluted peptides were dried down in a centrifugal evaporator, reconstituted in 5% formic acid and analyzed by nanospray LC-MS/MS on an Orbitrap Fusion mass spectrometer (Thermo Fisher). Peptides were separated by reverse-phase HPLC on a hand-packed column (packed with 40 cm of 1.8 µm, 120 Å pores, Sepax GP-C18, Sepax Technologies, Newark, DE) using an 85-minute gradient of 5-27% buffer B (ACN, 0.1% FA) at a 350 nl/min. Peptides were detected using a Top20 method. For each cycle, one full MS scan of m/z = 375–1400 was acquired in the Orbitrap at a resolution of 120,000 at m/z with AGC target = 5x105. Each full scan was followed by the selection of up to 20 of the most intense ions for CID and MS/MS analysis in the linear ion trap. Selected ions were excluded from further analysis for 30 s. Ions with charge 1+ or unassigned were also rejected. Maximum ion accumulation times were 100 ms for each full MS scan and 35 ms for MS/MS scans.

MS2 spectra were searched using SEQUEST against a composite database containing the translated sequences of 20,193 reviewed human protein sequences in the Universal Protein Resource (UniProt) database (downloaded March 18, 2016) and their reversed complement, using the following parameters: a precursor mass tolerance of ±20 ppm; 1.0 Da product ion mass tolerance; tryptic digestion; up to two missed cleavages; static modifications of carbamidomethylation on cysteine (+57.0214), and a dynamic modification of methionine oxidation (+15.9949). Peptide spectral matches were filtered to 1% FDR using the target-decoy strategy (101) combined with linear discriminant analysis (LDA) using SEQUEST scoring parameters including Xcorr, ΔCn′, precursor mass error, and charge state (102). In-house software was used to extract the peptide peak signal-to-noise ratio and area under the curve from the precursor MS1 scans. Label free protein abundance measurements were derived from the sum of these values for all unique peptides mapping to each protein.

Genetically Engineered Mice

Transgenic mice carrying an integrated CAG-LSL-MYCN gene at the *Rosa26* (R26) locus (kind gift from Johannes Schulte, Charité – Universitätsmedizin, Berlin, Germany (103)) were crossed with mice expressing Cre recombinase under the control of the probasin promoter and homozygously-floxed *Pten* alleles (kind gift from Yu Chen, Memorial Sloan-Kettering Cancer Center, New York, NY (104)). Following removal of the LSL cassette by Cre, a chicken actin promoter drives human N-Myc expression in these models. All lines of mice are bred on the same mixed genetic background (C57BL6/129x1/SvJ) and have been previously described (15). Mice were maintained and all procedures were performed on male mice following protocols approved by the WCM-IACUC (protocol no. 2008-0019).

Xenografts

22Rv1-CTL or 22Rv1-N-Myc cells were engineered to express luciferase using a transposable element vector (kind gift from John Ohlfest, University of Minnesota Medical School, Minneapolis, MN) and $1x10^6$ cells were injected into NU/J mice (Jackson Laboratories). Mice were surgically castrated once the tumor volume reached 150 mm^3. Mice were anesthetized with 4% isoflurane and the skin over the scrotum was disinfected by 70% ethanol and betadine solution. A 0.5-cm incision was made over the scrotum, the testes were exposed by pulling the adipose tissue, the blood vessels supplying the testis were cauterized, and the incision edges were closed with sterilized wound clips. Suture removal was performed between post-operative days 10-14.

Immunohistochemistry (IHC)

Formalin fixed paraffin embedded (FFPE) tissue sections were de-paraffinized and endogenous peroxidase was inactivated. Antigen retrieval was accomplished by the Bond Epitope Retrieval Solution 1 (Leica Biosystems, AR9961) at 99-100°C for 30 minutes. Following retrieval, the sections were incubated sequentially with the primary antibody for 25 minutes, post-primary for 15 minutes and polymer for 25 minutes ending with colorimetric development with diaminobenzidine (DAB) for 10 minutes using the Bond Polymer Refine Detection Kit (Leica Biosystems, DS9800). All histological evaluations and quantifications (including Hematoxylin and eosin (H&E)-stained and IHC images) were performed by a board-certified, genitourinary pathologist (B. Robinson) and follow criteria that have previously been described (105). Antibodies used were: Keratin 5 (Biolegend, 905501), AR (Abcam, ab108341), Vimentin (Santa Cruz, sc-7557), NCAM (Leica Biosystems, NCL-L-CD56-504), Keratin 8 (Developmental Studies Hybridoma Bank, AB_531826), S100 (Dako, Z0311).

In Situ Proximity Ligation Assay

The in situ proximity ligation assay (PLA) was conducted using the Duolink In Situ Red Starter Kit (Sigma-Aldrich, DUO92101) as recommended by the manufacturer. Fixed and saturated cells were incubated with antibodies against N-Myc (Santa Cruz, sc53993) and EZH2 (Active Motif, 39901). For enzalutamide treatment, cells were treated with 1 μM drug for 72 hours prior to PLA.

Gene Knockdown by Interfering RNA

For lentiviral shRNA transduction, human organoids or LNCaP-N-Myc cells were transduced using lentiviruses containing shRNA constructs against *EZH2* or *MYCN*, respectively. Organoids were dissociated with TrypLE (Gibco) and resuspended in organoid medium (84) containing Polybrene (Millipore) and Y27632 (Selleckchem, S1049). The dissociated organoid cells were combined with viral suspension and centrifugated at 600 x g, 32°C for 60 minutes. The organoid/virus mix was then incubated at 37°C overnight. Organoid cells were subsequently collected, resuspended in 120 µl of Matrigel (Corning) and seeded in a 24-well plate. Antibiotic selection was performed using 1 µg/ml puromycin (Thermo Scientific) for 7 days. LNCaP-N-Myc cells were transduced in 6-well plates in medium containing Polybrene (Millipore). Cells were selected with 2 µg/ml puromycin (Thermo Scientific) for 3 days.

For FOXA1 silencing, LNCaP cells were plated in T175 and 24 hours later cultured in phenol-red free RPMI medium (Gibco, 11835-030) supplemented with 5% charcoal stripped serum (Gibco, A33821-01) and 1% penicillin/streptomycin. Cells were transfected after 24 hours with siRNA FOXA1 or CTL (**Table S5**). Proteins and cells were collected and fixed 48 hours later for immunoblot and ChIP-QPCR.

MYCN RNA in situ hybridization (ISH)

RNA ISH was performed using the single-color chromogenic QuantiGene® ViewRNA ISH Tissue Assay Kit (Thermo Scientific, QVT0012) with a human MYCN ViewRNA Type 1 probe (Thermo Scientific, Assay ID: VA1-18174-VT, Cat #: VX-01) as previously described (15).

Data Availability

The ChIP-seq and RNA-seq generated in this paper have been deposited in the Gene Expression Omnibus (GEO) under accession numbers GSE117306, GSE117430, GSE117281 and GSE117282.

Statistics

Quantification

Quantitative data are presented as mean ± SEM unless otherwise indicated.

Statistical Analysis

Statistical analysis was performed using GraphPad Prism as described in the figure legends. * $p < 0.05$, ** $p < 0.01$, *** $p < 0.001$ unless otherwise indicated.

Study Approval

Animals

Mice were maintained and all procedures were performed on male mice following protocols approved by the WCM-IACUC (protocol no. 2008-0019).

Human Subjects

Male patients were enrolled on an Institutional Review Board (IRB)-approved protocol with informed consent (WCM IRB no. 1305013903 and 1210013164). For these studies, 29 benign prostate tissues, 66 localized prostate cancer, 73 metastatic castrate-resistant prostate adenocarcinoma, and 36 metastatic neuroendocrine prostate cancer were selected for further analysis.

Author Contributions

A.B. and N.J.B. share first authorship. A.B. initiated the experimental work including all of the ChIP-seq and validation experiments and remained involved throughout. N.J.B. performed essential computational analyses to define the N-Myc cistrome and to integrate cell line and mouse RNA-seq data, as well as performed and analyzed the RIME experiment. A.B. is named first because her contributions were made over a longer period than those of N.J.B.

A.B., N.J.B. and D.S.R. conceived and designed the experiments. A.B., N.J.B. and D.S.R. wrote the manuscript. A.B., N.J.B., E.D., M.A.A., A.A., X.L., I.H. and A.M.B. performed the experiments. A.B., N.J.B., R.B., B.R., V.C., M.A.A. and N.D. performed analysis and provided text. L.P., A.S., O.E., J.P., C.E.B., N.D., H.B. provided pre-clinical data and resources. H.B., O.E., B.R., N.D., J.Y. and J.P. supervised, supported analyses and edited the manuscript. B.R coordinated pathology, review and processing. H.B. coordinated patient sample collection and provided clinical samples, biospecimens, patient data and clinical expertise. D.S.R. supervised the study.

Acknowledgements

We thank the following Weill Cornell Medicine core facilities: The Translational Research Program in the Department of Pathology and Laboratory Medicine (Bing He, Yifang Liu, Leticia Dizon), the Genomics and Epigenomics cores (Dr. Jenny Xiang, Dr. Alicia Alonzo, Dr. Doron Betel), the Scientific Computing Unit, and the Englander Institute of Precision Medicine. This work was supported in part by USA Department of Defense Early Investigator Research Award (A.B., E.D., M.A.A., L.P.), Department of Defense Impact Award W81XWH-17-1-0652 (H.B, D.S.R.), National Cancer Institute (T32CA203702 (N.J.B.), SPORE Grant P50CA211024 (B.R., A.S., O.E., C.E.B., H.B., D.S.R.), K08CA187417 (C.E.B.), R01CA215040 (C.E.B.)), Urology Care Foundation Rising Star in Urology Research Award (C.E.B.), Damon Runyon Cancer Research Foundation MetLife Foundation Family Clinical Investigator Award (C.E.B.), National Institute on Aging Grant R01AG048284 (J.P.), Prostate Cancer Foundation Young Investigator Award (M.A.A., L.P.) and Prostate Cancer Foundation Challenge Award (O.E., H.B., D.S.R.). Enzalutamide was provided by Astellas Pharma Inc. (Northbrook, IL) and Medivation, Inc. (San Francisco, CA).

References

1. Beltran H, et al. Divergent clonal evolution of castration-resistant neuroendocrine prostate cancer. *Nat Med.* 2016;22(3):298-305.

2. Niederst MJ, et al. RB loss in resistant EGFR mutant lung adenocarcinomas that transform to small-cell lung cancer. *Nat Commun.* 2015;6:6377.

3. Sequist LV, et al. Genotypic and histological evolution of lung cancers acquiring resistance to EGFR inhibitors. *Sci Transl Med.* 2011;3(75):75ra26.

4. Aparicio A, et al. Neuroendocrine prostate cancer xenografts with large-cell and small-cell features derived from a single patient's tumor: morphological, immunohistochemical, and gene expression profiles. *Prostate.* 2011;71(8):846-856.

5. Tzelepi V, et al. Modeling a lethal prostate cancer variant with small-cell carcinoma features. *Clin Cancer Res.* 2012;18(3):666-677.

6. Aparicio AM, et al. Combined Tumor Suppressor Defects Characterize Clinically Defined Aggressive Variant Prostate Cancers. *Clin Cancer Res.* 2016;22(6):1520-1530.

7. Ku SY, et al. Rb1 and Trp53 cooperate to suppress prostate cancer lineage plasticity, metastasis, and antiandrogen resistance. *Science.* 2017;355(6320):78-83.

8. Martin P, et al. Prostate epithelial Pten/TP53 loss leads to transformation of multipotential progenitors and epithelial to mesenchymal transition. *Am J Pathol.* 2011;179(1):422-435.

9. Mu P, et al. SOX2 promotes lineage plasticity and antiandrogen resistance in TP53- and RB1-deficient prostate cancer. *Science.* 2017;355(6320):84-88.

10. Tan HL, et al. Rb loss is characteristic of prostatic small cell neuroendocrine carcinoma. *Clin Cancer Res.* 2014;20(4):890-903.

11. Zhou Z, et al. Synergy of p53 and Rb deficiency in a conditional mouse model for metastatic prostate cancer. *Cancer Res.* 2006;66(16):7889-7898.

12. Zou M, et al. Transdifferentiation as a Mechanism of Treatment Resistance in a Mouse Model of Castration-resistant Prostate Cancer. *Cancer Discov.* 2017;7(7):736-749.

13. Zhang X, et al. SRRM4 Expression and the Loss of REST Activity May Promote the Emergence of the Neuroendocrine Phenotype in Castration-Resistant Prostate Cancer. *Clin Cancer Res.* 2015;21(20):4698-4708.

14. Beltran H, et al. Molecular characterization of neuroendocrine prostate cancer and identification of new drug targets. *Cancer Discov.* 2011;1(6):487-495.

15. Dardenne E, et al. N-Myc Induces an EZH2-Mediated Transcriptional Program Driving Neuroendocrine Prostate Cancer. *Cancer Cell.* 2016;30(4):563-577.

16. Lee JK, et al. N-Myc Drives Neuroendocrine Prostate Cancer Initiated from Human Prostate Epithelial Cells. *Cancer Cell.* 2016;29(4):536-547.

17. Mosquera JM, et al. Concurrent AURKA and MYCN gene amplifications are harbingers of lethal treatment-related neuroendocrine prostate cancer. *Neoplasia.* 2013;15(1):1-10.

18. Bishop JL, et al. The Master Neural Transcription Factor BRN2 Is an Androgen Receptor-Suppressed Driver of Neuroendocrine Differentiation in Prostate Cancer. *Cancer Discov.* 2017;7(1):54-71.

19. Davis FG, McCarthy BJ, Freels S, Kupelian V, Bondy ML. The conditional probability of survival of patients with primary malignant brain tumors: surveillance, epidemiology, and end results (SEER) data. *Cancer.* 1999;85(2):485-491.

20. Garson JA, McIntyre PG, Kemshead JT. N-myc amplification in malignant astrocytoma. *Lancet.* 1985;2(8457):718-719.

21. Lee WH, Murphree AL, Benedict WF. Expression and amplification of the N-myc gene in primary retinoblastoma. *Nature.* 1984;309(5967):458-460.

22. Marshall GM, et al. The prenatal origins of cancer. *Nat Rev Cancer.* 2014;14(4):277-289.

23. Northcott PA, et al. Medulloblastomics: the end of the beginning. *Nat Rev Cancer.* 2012;12(12):818-834.

24. Swartling FJ, et al. Distinct neural stem cell populations give rise to disparate brain tumors in response to N-MYC. *Cancer Cell.* 2012;21(5):601-613.

25. Driman D, Thorner PS, Greenberg ML, Chilton-MacNeill S, Squire J. MYCN gene amplification in rhabdomyosarcoma. *Cancer.* 1994;73(8):2231-2237.

26. Fielitz K, et al. Characterization of pancreatic glucagon-producing tumors and pituitary gland tumors in transgenic mice overexpressing MYCN in hGFAP-positive cells. *Oncotarget.* 2016;7:74415-74426.

27. Hirvonen H, Hukkanen V, Salmi TT, Pelliniemi TT, Alitalo R. L-myc and N-myc in hematopoietic malignancies. *Leuk Lymphoma.* 1993;11(3-4):197-205.

28. Kawagoe H, Grosveld GC. Conditional MN1-TEL knock-in mice develop acute myeloid leukemia in conjunction with overexpression of HOXA9. *Blood.* 2005;106(13):4269-4277.

29. King B, et al. The ubiquitin ligase Huwe1 regulates the maintenance and lymphoid commitment of hematopoietic stem cells. *Nat Immunol.* 2016;17(11):1312-1321.

30. Nau MM, et al. Human small-cell lung cancers show amplification and expression of the N-myc gene. *Proc Natl Acad Sci U S A.* 1986;83(4):1092-1096.

31. van Lohuizen M, Breuer M, Berns A. N-myc is frequently activated by proviral insertion in MuLV-induced T cell lymphomas. *EMBO J.* 1989;8(1):133-136.

32. Williams RD, et al. Molecular profiling reveals frequent gain of MYCN and anaplasia-specific loss of 4q and 14q in Wilms tumor. *Genes Chromosomes Cancer.* 2011;50(12):982-995.

33. Williamson D, et al. Relationship between MYCN copy number and expression in rhabdomyosarcomas and correlation with adverse prognosis in the alveolar subtype. *J Clin Oncol.* 2005;23(4):880-888.

34. Rickman DS, Schulte JH, Eilers M. The Expanding World of N-MYC-Driven Tumors. *Cancer Discov.* 2018;8(2):150-163.

35. Kerkhoff E, Bister K, Klempnauer KH. Sequence-specific DNA binding by Myc proteins. *Proc Natl Acad Sci U S A.* 1991;88(10):4323-4327.

36. Dang CV. MYC on the path to cancer. *Cell.* 2012;149(1):22-35.

37. Epstein JI, et al. Proposed morphologic classification of prostate cancer with neuroendocrine differentiation. *Am J Surg Pathol.* 2014;38(6):756-767.

38. Lee G, et al. Isolation and directed differentiation of neural crest stem cells derived from human embryonic stem cells. *Nat Biotechnol.* 2007;25(12):1468-1475.

39. Subramanian A, et al. Gene set enrichment analysis: a knowledge-based approach for interpreting genome-wide expression profiles. *Proc Natl Acad Sci U S A.* 2005;102(43):15545-15550.

40. Bhattacharya B, et al. Gene expression in human embryonic stem cell lines: unique molecular signature. *Blood.* 2004;103(8):2956-2964.

41. Dulken BW, Leeman DS, Boutet SC, Hebestreit K, Brunet A. Single-Cell Transcriptomic Analysis Defines Heterogeneity and Transcriptional Dynamics in the Adult Neural Stem Cell Lineage. *Cell Rep.* 2017;18(3):777-790.

42. Parimi V, Goyal R, Poropatich K, Yang XJ. Neuroendocrine differentiation of prostate cancer: a review. *Am J Clin Exp Urol.* 2014;2(4):273-285.

43. Weiss WA, Aldape K, Mohapatra G, Feuerstein BG, Bishop JM. Targeted expression of MYCN causes neuroblastoma in transgenic mice. *EMBO J.* 1997;16(11):2985-2995.

44. Meissner A, et al. Genome-scale DNA methylation maps of pluripotent and differentiated cells. *Nature.* 2008;454(7205):766-770.

45. Mikkelsen TS, et al. Genome-wide maps of chromatin state in pluripotent and lineage-committed cells. *Nature.* 2007;448(7153):553-560.

46. Chen Z, et al. Diverse AR-V7 cistromes in castration-resistant prostate cancer are governed by HoxB13. *Proc Natl Acad Sci U S A.* 2018;115(26):6810-6815.

47. Smith BA, et al. A Human Adult Stem Cell Signature Marks Aggressive Variants across Epithelial Cancers. *Cell Rep.* 2018;24(12):3353-3366 e3355.

48. Zeid R, et al. Enhancer invasion shapes MYCN-dependent transcriptional amplification in neuroblastoma. *Nat Genet.* 2018;50(4):515-523.

49. Guo J, et al. Sequence specificity incompletely defines the genome-wide occupancy of Myc. *Genome Biol.* 2014;15(10):482.

50. Lorenzin F, et al. Different promoter affinities account for specificity in MYC-dependent gene regulation. *Elife.* 2016;5:e15161.

51. Kron KJ, et al. TMPRSS2-ERG fusion co-opts master transcription factors and activates NOTCH signaling in primary prostate cancer. *Nat Genet.* 2017;49(9):1336-1345.

52. Pomerantz MM, et al. The androgen receptor cistrome is extensively reprogrammed in human prostate tumorigenesis. *Nat Genet.* 2015;47(11):1346-1351.

53. Wang Q, et al. A hierarchical network of transcription factors governs androgen receptor-dependent prostate cancer growth. *Mol Cell.* 2007;27(3):380-392.

54. Wang Q, et al. Androgen receptor regulates a distinct transcription program in androgen-independent prostate cancer. *Cell.* 2009;138(2):245-256.

55. Zhao JC, Fong KW, Jin HJ, Yang YA, Kim J, Yu J. FOXA1 acts upstream of GATA2 and AR in hormonal regulation of gene expression. *Oncogene.* 2016;35(33):4335-4344.

56. Mohammed H, Taylor C, Brown GD, Papachristou EK, Carroll JS, D'Santos CS. Rapid immunoprecipitation mass spectrometry of endogenous proteins (RIME) for analysis of chromatin complexes. *Nat Protoc.* 2016;11(2):316-326.

57. Blackwood EM, Eisenman RN. Max: a helix-loop-helix zipper protein that forms a sequence-specific DNA-binding complex with Myc. *Science.* 1991;251(4998):1211-1217.

58. Buchel G, et al. Association with Aurora-A Controls N-MYC-Dependent Promoter Escape and Pause Release of RNA Polymerase II during the Cell Cycle. *Cell Rep.* 2017;21(12):3483-3497.

59. McMahon SB, Van Buskirk HA, Dugan KA, Copeland TD, Cole MD. The novel ATM-related protein TRRAP is an essential cofactor for the c-Myc and E2F oncoproteins. *Cell.* 1998;94(3):363-374.

60. Bernstein BE, et al. A bivalent chromatin structure marks key developmental genes in embryonic stem cells. *Cell.* 2006;125(2):315-326.

61. Gao Y, Gan H, Lou Z, Zhang Z. Asf1a resolves bivalent chromatin domains for the induction of lineage-specific genes during mouse embryonic stem cell differentiation. *Proc Natl Acad Sci U S A.* 2018;115(27):E6162-E6171.

62. Hanakawa Y, Amagai M, Shirakata Y, Sayama K, Hashimoto K. Different effects of dominant negative mutants of desmocollin and desmoglein on the cell-cell adhesion of keratinocytes. *J Cell Sci.* 2000;113 (Pt 10):1803-1811.

63. Haddox CL, et al. Blinatumomab-induced lineage switch of B-ALL with t(4:11)(q21;q23) KMT2A/AFF1 into an aggressive AML: pre- and post-switch phenotypic, cytogenetic and molecular analysis. *Blood Cancer J.* 2017;7(9):e607.

64. Rickman DS, Beltran H, Demichelis F, Rubin MA. Biology and evolution of poorly differentiated neuroendocrine tumors. *Nat Med.* 2017;23(6):1-10.

65. Tata PR, et al. Developmental History Provides a Roadmap for the Emergence of Tumor Plasticity. *Dev Cell.* 2018;44(6):679-693.

66. Malta TM, et al. Machine Learning Identifies Stemness Features Associated with Oncogenic Dedifferentiation. *Cell.* 2018;173(2):338-354 e315.

67. Park JW, et al. Reprogramming normal human epithelial tissues to a common, lethal neuroendocrine cancer lineage. *Science.* 2018;362(6410):91-95.

68. Huang C, et al. Cbx3 maintains lineage specificity during neural differentiation. *Genes Dev.* 2017;31(3):241-246.

69. Gurel B, et al. Nuclear MYC protein overexpression is an early alteration in human prostate carcinogenesis. *Mod Pathol.* 2008;21(9):1156-1167.

70. Clegg NJ, et al. MYC cooperates with AKT in prostate tumorigenesis and alters sensitivity to mTOR inhibitors. *PLoS One.* 2011;6(3):e17449.

71. Ellwood-Yen K, et al. Myc-driven murine prostate cancer shares molecular features with human prostate tumors. *Cancer Cell.* 2003;4(3):223-238.

72. Koh CM, Bieberich CJ, Dang CV, Nelson WG, Yegnasubramanian S, De Marzo AM. MYC and Prostate Cancer. *Genes Cancer.* 2010;1(6):617-628.

73. Huijbers IJ, et al. Rapid target gene validation in complex cancer mouse models using re-derived embryonic stem cells. *EMBO Mol Med.* 2014;6(2):212-225.

74. Kim DW, et al. Genetic requirement for Mycl and efficacy of RNA Pol I inhibition in mouse models of small cell lung cancer. *Genes Dev.* 2016;30(11):1289-1299.

75. Mollaoglu G, et al. MYC Drives Progression of Small Cell Lung Cancer to a Variant Neuroendocrine Subtype with Vulnerability to Aurora Kinase Inhibition. *Cancer Cell.* 2017;31(2):270-285.

76. Peifer M, et al. Integrative genome analyses identify key somatic driver mutations of small-cell lung cancer. *Nat Genet.* 2012;44(10):1104-1110.

77. Rudin CM, Poirier JT. MYC, MAX, and small cell lung cancer. *Cancer Discov.* 2014;4(3):273-274.

78. Sos ML, et al. A framework for identification of actionable cancer genome dependencies in small cell lung cancer. *Proc Natl Acad Sci U S A.* 2012;109(42):17034-17039.

79. Wong AJ, Ruppert JM, Eggleston J, Hamilton SR, Baylin SB, Vogelstein B. Gene amplification of c-myc and N-myc in small cell carcinoma of the lung. *Science.* 1986;233(4762):461-464.

80. Bergmann F, et al. Acinar cell carcinomas of the pancreas: a molecular analysis in a series of 57 cases. *Virchows Arch.* 2014;465(6):661-672.

81. Skoudy A, Hernandez-Munoz I, Navarro P. Pancreatic ductal adenocarcinoma and transcription factors: role of c-Myc. *J Gastrointest Cancer.* 2011;42(2):76-84.

82. Aggarwal R, et al. Clinical and Genomic Characterization of Treatment-Emergent Small-Cell Neuroendocrine Prostate Cancer: A Multi-institutional Prospective Study. *J Clin Oncol.* 2018:JCO2017776880.

83. Bluemn EG, et al. Androgen Receptor Pathway-Independent Prostate Cancer Is Sustained through FGF Signaling. *Cancer Cell.* 2017;32(4):474-489.

84. Puca L, et al. Patient derived organoids to model rare prostate cancer phenotypes. *Nat Commun.* 2018;9(1):2404.

85. Chakravarty D, et al. The oestrogen receptor alpha-regulated lncRNA NEAT1 is a critical modulator of prostate cancer. *Nat Commun.* 2014;5:5383.

86. Beltran H, et al. Whole-Exome Sequencing of Metastatic Cancer and Biomarkers of Treatment Response. *JAMA Oncol.* 2015;1(4):466-474.

87. Bolger AM, Lohse M, Usadel B. Trimmomatic: a flexible trimmer for Illumina sequence data. *Bioinformatics.* 2014;30(15):2114-2120.

88. Dobin A, et al. STAR: ultrafast universal RNA-seq aligner. *Bioinformatics.* 2013;29(1):15-21.

89. Li H, et al. The Sequence Alignment/Map format and SAMtools. *Bioinformatics.* 2009;25(16):2078-2079.

90. Trapnell C, et al. Differential gene and transcript expression analysis of RNA-seq experiments with TopHat and Cufflinks. *Nat Protoc.* 2012;7(3):562-578.

91. Anders S, Pyl PT, Huber W. HTSeq--a Python framework to work with high-throughput sequencing data. *Bioinformatics.* 2015;31(2):166-169.

92. Love MI, Huber W, Anders S. Moderated estimation of fold change and dispersion for RNA-seq data with DESeq2. *Genome Biol.* 2014;15(12):550.

93. Johnson WE, Li C, Rabinovic A. Adjusting batch effects in microarray expression data using empirical Bayes methods. *Biostatistics.* 2007;8(1):118-127.

94. Leek JT, Johnson WE, Parker HS, Jaffe AE, Storey JD. The sva package for removing batch effects and other unwanted variation in high-throughput experiments. *Bioinformatics.* 2012;28(6):882-883.

95. Langmead B, Salzberg SL. Fast gapped-read alignment with Bowtie 2. *Nat Methods.* 2012;9(4):357-359.

96. Zhang Y, et al. Model-based analysis of ChIP-Seq (MACS). *Genome Biol.* 2008;9(9):R137.

97. Heinz S, et al. Simple combinations of lineage-determining transcription factors prime cis-regulatory elements required for macrophage and B cell identities. *Mol Cell.* 2010;38(4):576-589.

98. Quinlan AR, Hall IM. BEDTools: a flexible suite of utilities for comparing genomic features. *Bioinformatics.* 2010;26(6):841-842.

99. Ramirez F, et al. deepTools2: a next generation web server for deep-sequencing data analysis. *Nucleic Acids Res.* 2016;44(W1):W160-165.

100. Rappsilber J, Ishihama Y, Mann M. Stop and go extraction tips for matrix-assisted laser desorption/ionization, nanoelectrospray, and LC/MS sample pretreatment in proteomics. *Anal Chem.* 2003;75(3):663-670.

101. Elias JE, Gygi SP. Target-decoy search strategy for increased confidence in large-scale protein identifications by mass spectrometry. *Nat Methods.* 2007;4(3):207-214.

102. Huttlin EL, et al. A tissue-specific atlas of mouse protein phosphorylation and expression. *Cell.* 2010;143(7):1174-1189.

103. Althoff K, et al. A Cre-conditional MYCN-driven neuroblastoma mouse model as an improved tool for preclinical studies. *Oncogene.* 2015;34(26):3357-3368.

104. Chen Y, et al. ETS factors reprogram the androgen receptor cistrome and prime prostate tumorigenesis in response to PTEN loss. *Nat Med.* 2013;19(8):1023-1029.

105. Ittmann M, et al. Animal models of human prostate cancer: the consensus report of the New York meeting of the Mouse Models of Human Cancers Consortium Prostate Pathology Committee. *Cancer Res.* 2013;73(9):2718-2736.

Figures and Figure Legends

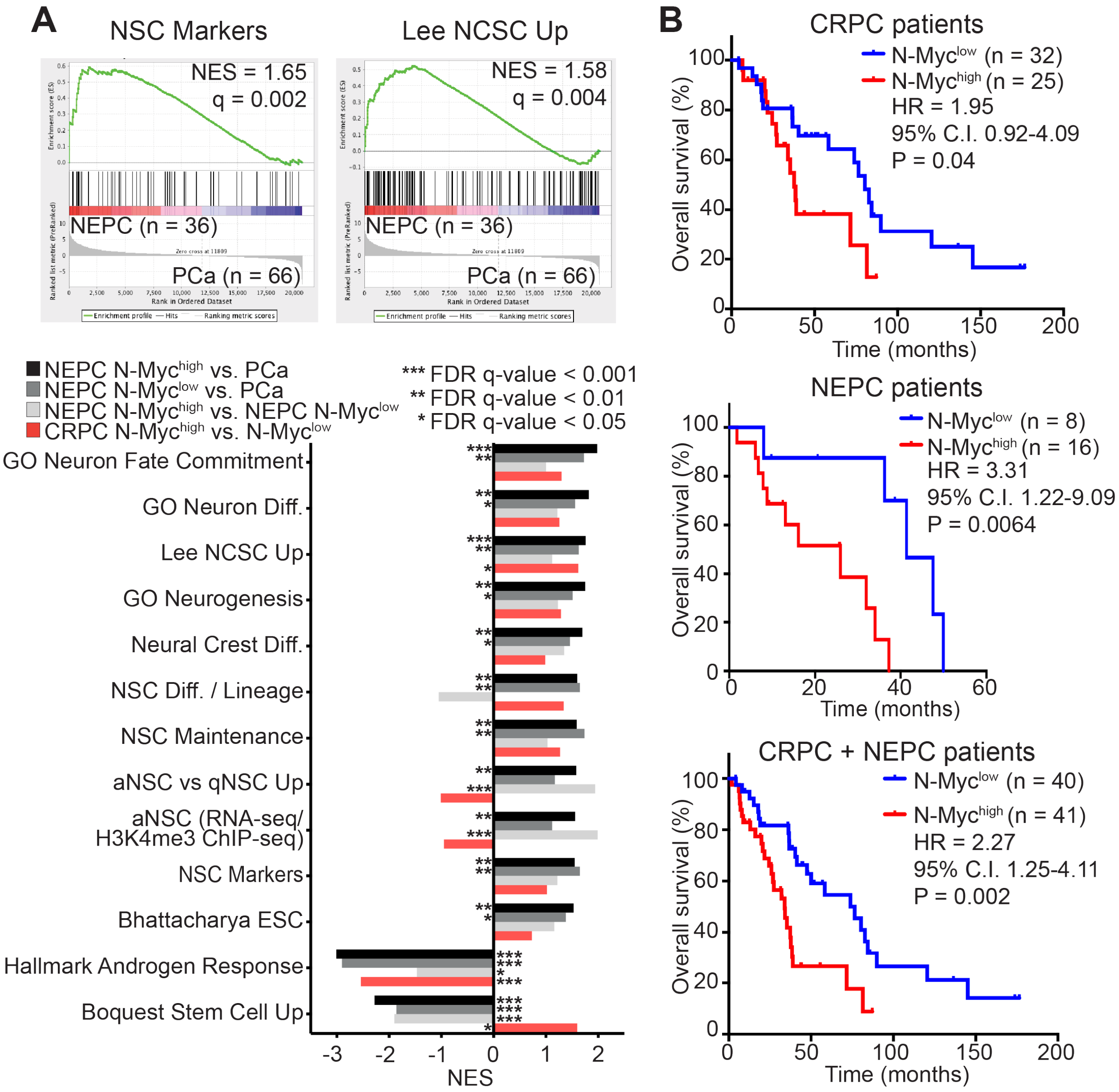

Figure 1. Clinical NEPC is associated with neural lineage.
(A) Top: Enrichment plots of the Neural Stem Cell Markers and Lee Neural Crest Stem Cell Up genesets between indicated groups. Bottom: Targeted GSEA in the five NEPC samples with the highest (N-Myc^{high}) or lowest (N-Myc^{low}) level of *MYCN* expression versus PCa (n = 66) patient samples, NEPC N-Myc^{high} versus NEPC N-Myc^{low}, and on the five CRPC with the highest level of *MYCN* expression versus the five lowest. **(B)** Kaplan–Meier plots of CRPC (n = 57) patients, NEPC (n = 24) patients or CRPC+NEPC (n = 81) patients, stratified into two categories according to the median value of *MYCN* mRNA expression. Survival analysis was performed using the Kaplan-Meier estimator (log-rank test).

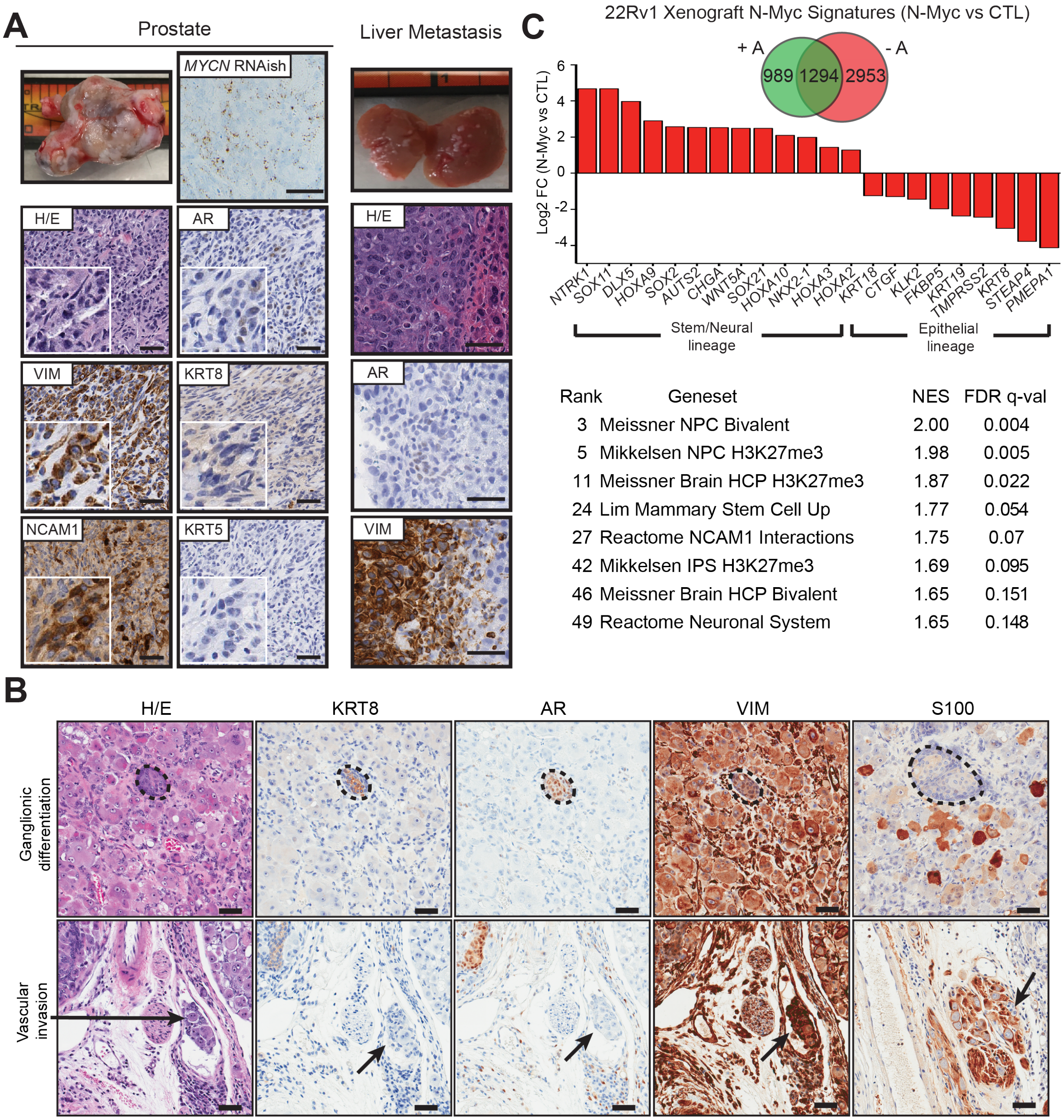

Rank	Geneset	NES	FDR q-val
3	Meissner NPC Bivalent	2.00	0.004
5	Mikkelsen NPC H3K27me3	1.98	0.005
11	Meissner Brain HCP H3K27me3	1.87	0.022
24	Lim Mammary Stem Cell Up	1.77	0.054
27	Reactome NCAM1 Interactions	1.75	0.07
42	Mikkelsen IPS H3K27me3	1.69	0.095
46	Meissner Brain HCP Bivalent	1.65	0.151
49	Reactome Neuronal System	1.65	0.148

Figure 2. AR signaling alters the N-Myc transcriptome in vivo.

(A) Photomicrograph images of Hematoxylin and Eosin (H/E) staining, vimentin (VIM), NCAM1, AR, cytokeratin 8 (KRT8) and 5 (KRT5) immunohistochemistry on primary prostate tumor region enriched with sarcomatoid differentiation (left) or liver metastatic lesion (right) from *Pb-Cre*$^{+/-}$; *Pten*$^{f/f}$; *LSL-MYCN*$^{+/+}$mice 6 months after castration (scale bar = 50 µm). **(B)** Photomicrograph images of H/E staining or IHC staining for epithelial markers (AR and KRT8), a mesenchymal (vimentin (VIM)) or neural/ganglionic marker (S100) on 4µm serial sections from mouse C1 **(Fig. S2)**. Dotted lines indicate conventional adenocarcinoma adjacent to neural/ganglionic cells. Arrows indicate VIM/S100 positive tumor cells that have invaded local vasculature. (scale bar = 50µm) **(C)** Top: N-Myc signatures defined from 22Rv1-N-Myc xenografts versus 22Rv1 control (CTL) xenografts (-1 < log2(fold change) < 1, adj. p-value < 0.05, n = 3 biological replicates per condition). Bottom: GSEA analysis results comparing N-Myc castrated tumors versus the other 3 groups of tumors.

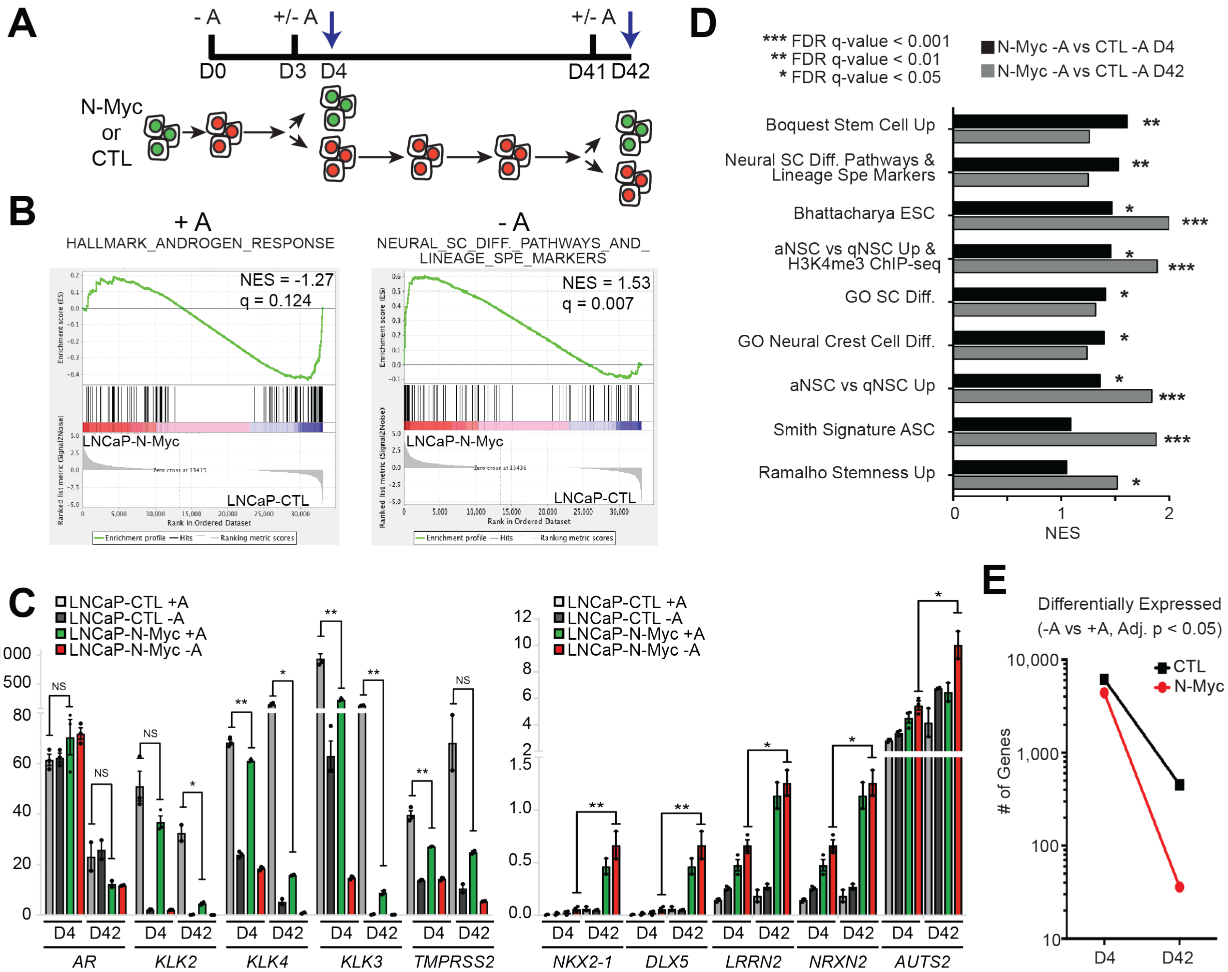

Figure 3. N-Myc expression leads to neural lineage gene expression and reduced androgen response.
(A) Experimental schematic with LNCaP-N-Myc or CTL cells and corresponding time points for RNA-seq or ChIP-seq analyses (arrows) in the presence (+A, green) or absence (-A, red) of androgen. **(B)** Enrichment plots for the Androgen Response and the Neural Stem Cell Differentiation Pathways and Lineage-specific Markers genesets from indicated conditions. **(C)** Gene expression (FPKM) of AR target genes (left) and neural lineage-associated genes (right) measured by RNA-seq in the indicated cells and conditions, at day 4 (D4, n = 3 biological replicates) and day 42 (D42, n = 2 biological replicates) of androgen withdrawal. * $p < 0.05$, ** $p < 0.01$, Sidak-Bonferroni adjusted two-tailed t-test. **(D)** Targeted GSEA on RNA-seq data from LNCaP-N-Myc versus CTL cells, without androgen, at D4 or D42 as indicated. **(E)** Number of genes differentially expressed (adj. p-value < 0.05) in the indicated conditions.

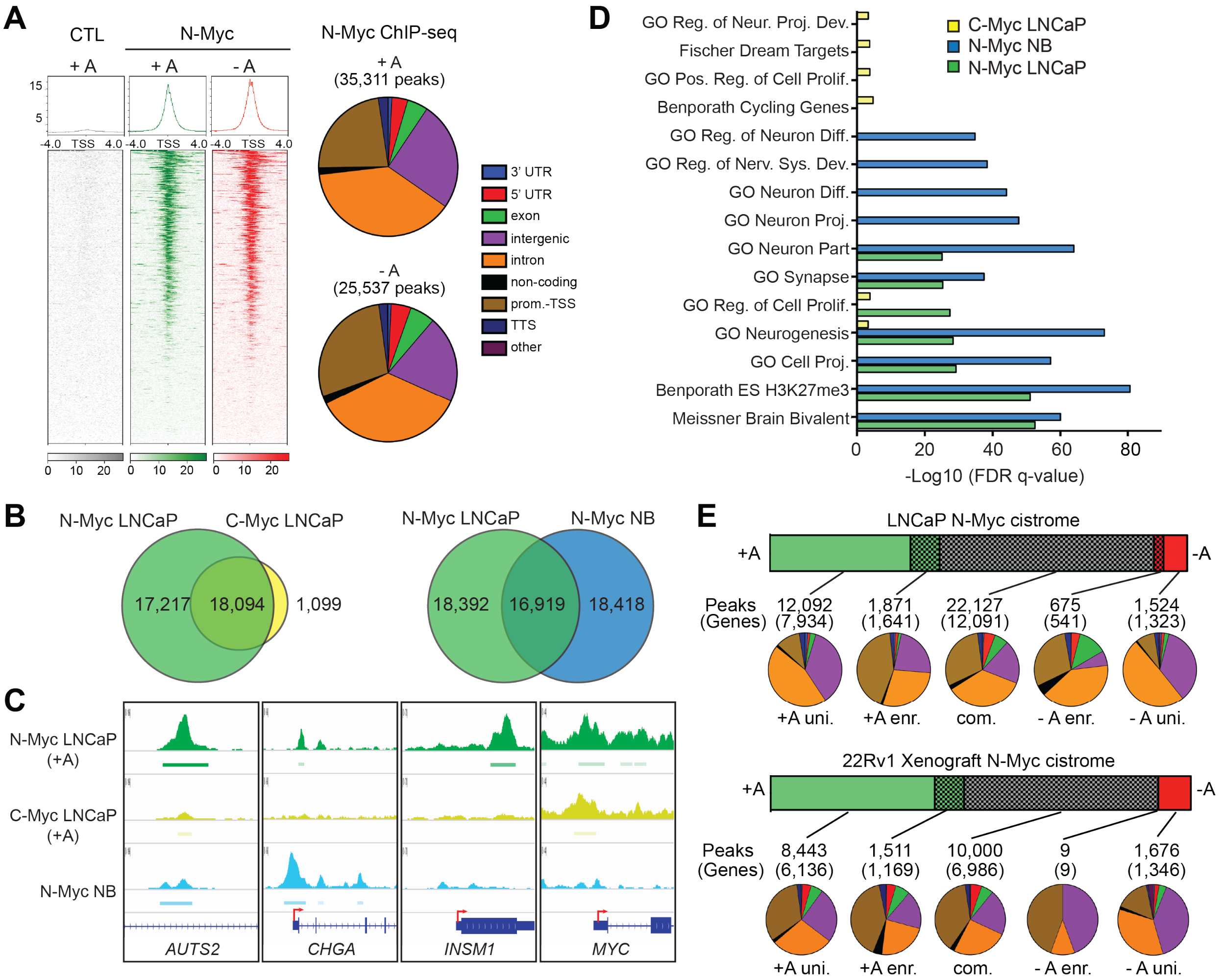

Figure 4. The N-Myc cistrome is distinct from C-Myc and is altered by androgen signaling.
(A) Left: Distributions and heatmaps of N-Myc ChIP-seq data generated from cells at day 4 (D4). Right: Proportion of N-Myc-bound sites at the indicated genomic annotation. **(B)** Overlap of Myc family member binding in prostate cancer cells (LNCaP, left) or N-Myc in prostate cancer cells versus published N-Myc in neuroblastoma cells (LNCaP/BE2C, right). **(C)** Examples of ChIP-seq tracks for indicated genes. **(D)** GSEA performed on the uniquely bound genes as identified in **(B)**. **(E)** Representation of N-Myc binding sites determined by ChIP-seq in LNCaP-N-Myc cells with and without androgen (top) or in 22Rv1 xenografts grown in castrated or intact recipients (bottom), and their distribution throughout the genome (n = 2 biological replicates per condition).

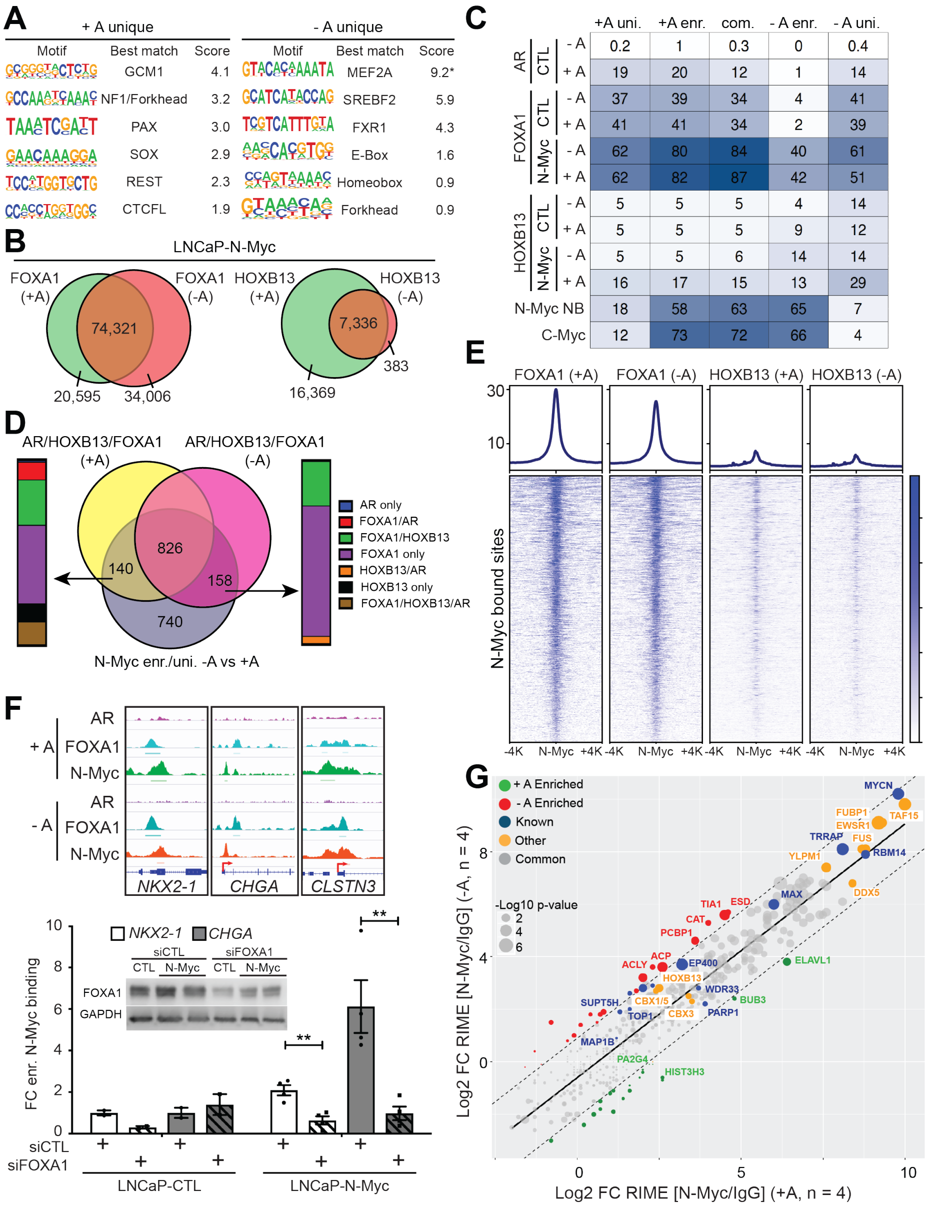

Figure 5. N-Myc interacts with known AR co-factors to alter DNA binding.
(A) Motif analysis of unique N-Myc peaks with or without androgen obtained by ChIP-seq in LNCaP-N-Myc cells. Scores correspond to log2 (% target / % background). All motifs shown are enriched with a p-value $< 10^{-5}$ and are listed with their best predicted match to a known protein family. * % background of MEF2A motif was 0% and was subsequently adjusted to 0.001% to calculate a score. **(B)** Overlap between FOXA1 or HOXB13 ChIP-seq peaks in the LNCaP-N-Myc cells in the presence or absence of androgen at day 4. **(C)** Comparison of N-Myc binding with AR (GSE69045), FOXA1 (CTL cells: GSE69045) and HOXB13 binding with or without androgen, N-Myc in BE2C neuroblastoma cells (GSE80151) and C-Myc in LNCaP. Numbers represent the percentage of N-Myc peaks in each condition overlapping with the indicated co-factor. **(D)** Overlap of N-Myc peaks (enriched and unique in -A) with AR, HOXB13 or FOXA1 peaks in the indicated conditions. **(E)** Distribution of FOXA1 and HOXB13 binding at N-Myc bound sites +/- 4Kb in the indicated conditions. **(F)** Top: ChIP-seq tracks of genes co-bound by N-Myc and FOXA1, independently of AR (in CTL cells), in the indicated conditions. Bottom: Effect of FOXA1 knockdown by siRNA (see Western blot inset) on N-Myc binding assessed by ChIP-qPCR. ** $p < 0.01$ Sidak-Bonferroni adjusted two-tailed t-test. **(G)** Scatter plot of log2(fold change of N-Myc bound peptides versus IgG-bound peptides, identified by RIME) with (X-axis) and without (Y-axis) androgen ($n = 4$ biological replicates per condition). Lines correspond to the regression line +/- 1.7 Z.

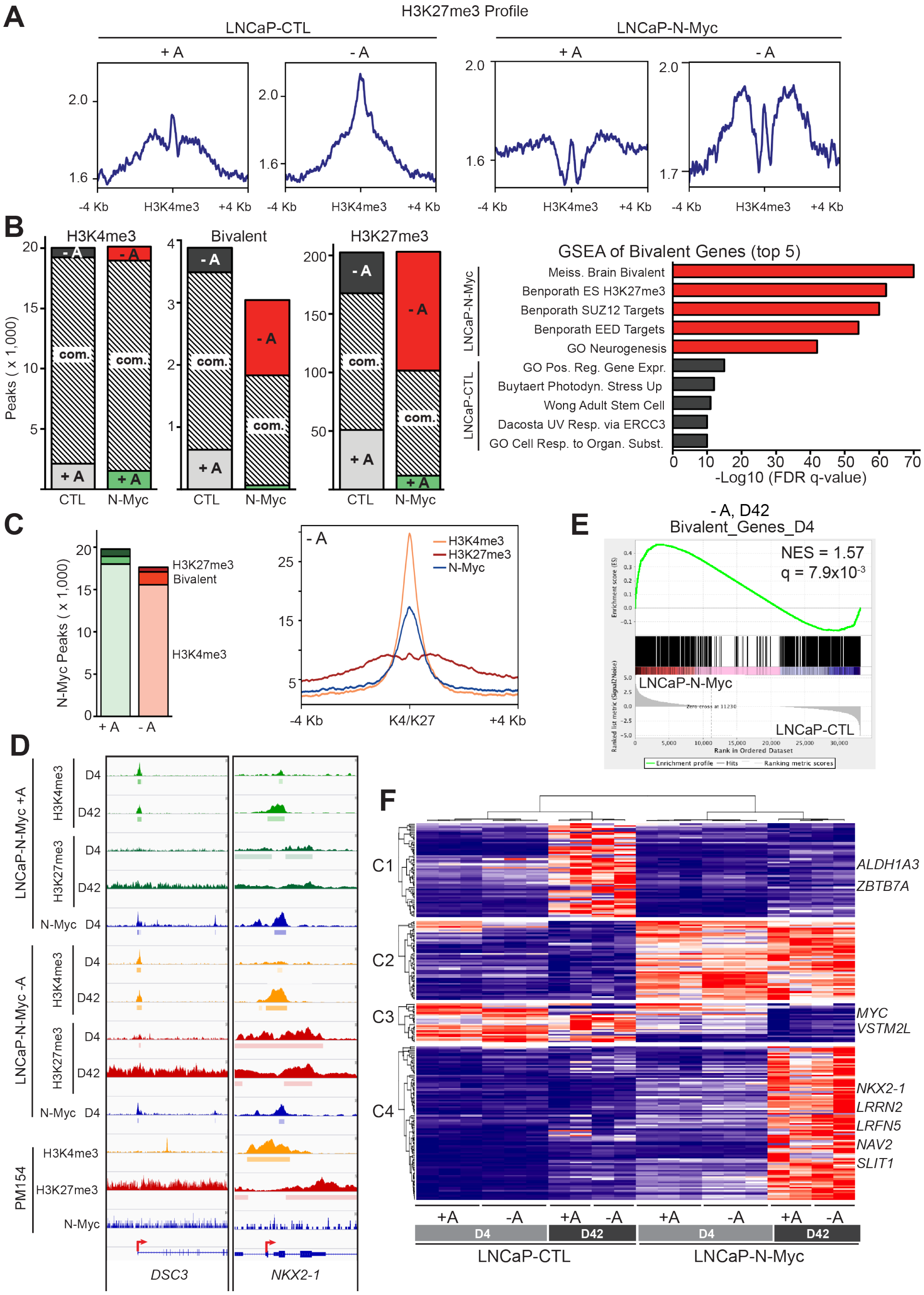

Figure 6. N-Myc promotes bivalency on neural lineage genes.
(A) H3K27me3 binding profiles within 8Kb centered at H3K4me3 peaks in LNCaP CTL and N-Myc cells, with and without androgen as specified. **(B)** Left: Number of H3K4me3, H3K27me3 or H3K4me3/H3K27me3 bivalent peaks in common or unique to the conditions at D4 as indicated. Right: Top 5 genesets from GSEA for uniquely bivalently marked genes in the absence of androgen from LNCaP-N-Myc cells (red) or CTL cells (black). **(C)** Left: Number of H3K4me3, H3K27me3 and bivalent peaks also bound by N-Myc with or without androgen. Right: H3K4me3, H3K27me3 and N-Myc binding profiles on bivalent peaks within 8Kb centered at H3K4me3 peaks, in LNCaP-N-Myc cells in the absence of androgen. **(D)** Examples of N-Myc and histone mark ChIP-seq tracks as indicated. **(E)** Enrichment plot of the bivalent genes identified in LNCaP-N-Myc -A cells at D4 measured in LNCaP-N-Myc -A cells vs LNCaP-CTL -A cells at D42. **(F)** Unsupervised clustering of the genes that were bivalent at D4 and differentially expressed (adj. $p < 0.05$) between LNCaP-N-Myc and LNCaP-CTL cells without androgen at D42.

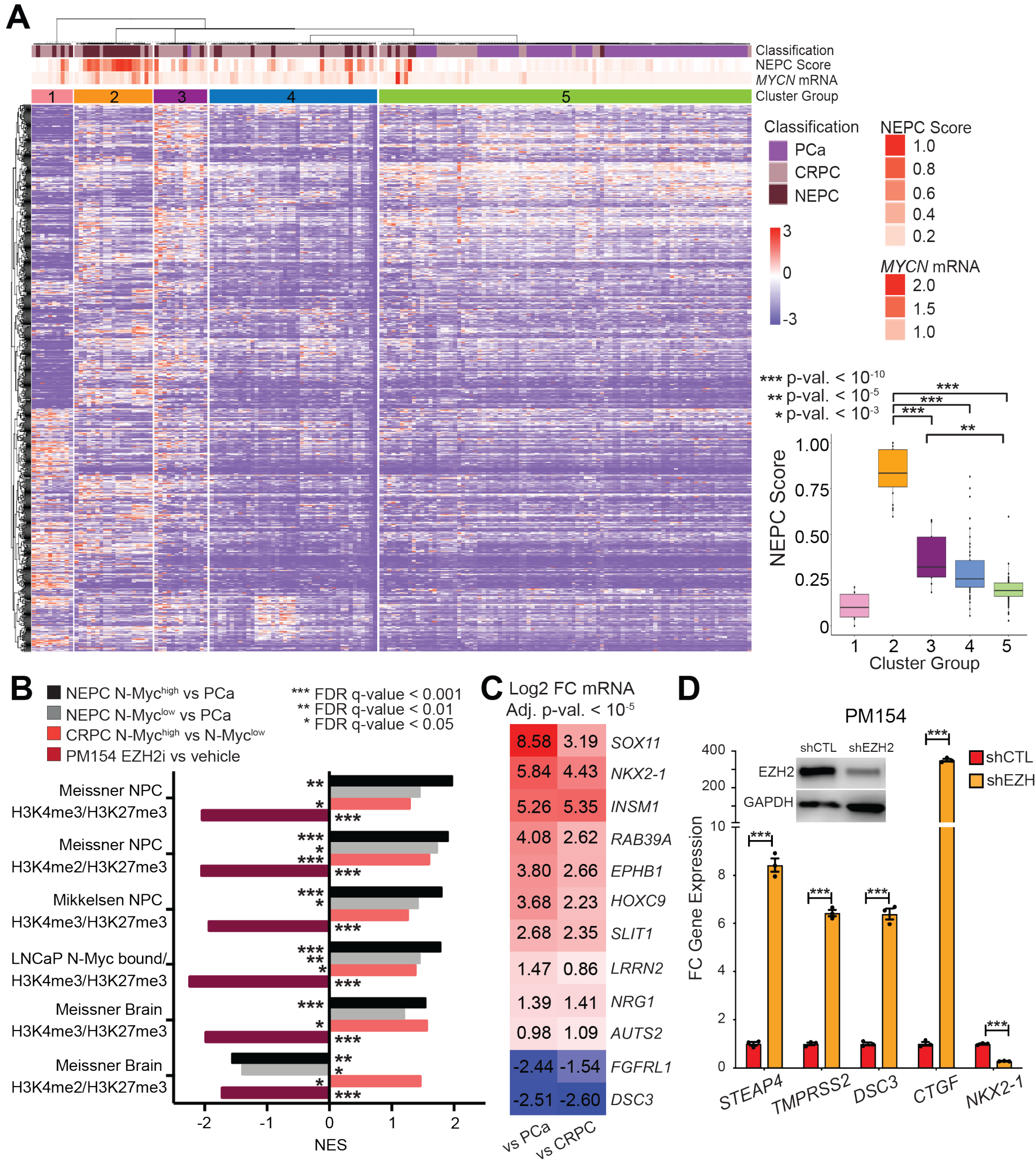

Figure 7. N-Myc-induced bivalent genes are clinically relevant.

(A) Top: Unsupervised clustering of PCa (n = 66), CRPC (n = 73) and NEPC (n = 36) patient samples based on the expression level of the 966 bivalent and N-Myc bound genes in LNCaP-N-Myc cells at D4 without androgen. Bottom: NEPC score for each cluster group. Graph depicts the median value between the 25th and 75th percentiles with whiskers indicating the range within 1.5 IQR, Student's unpaired two-tailed t-test. **(B)** Targeted GSEA of bivalent-related genesets in the five NEPC samples with the highest (N-Myc^{high}) or lowest (N-Myc^{low}) level of *MYCN* expression versus PCa (n = 66) patient samples, on the five CRPC with the highest level of *MYCN* expression versus the five lowest, and on PM154 cells treated with an EZH2 inhibitor versus vehicle. **(C)** Heatmap of log2(fold change) of genes in NEPC (n = 36) versus PCa (n = 66) or NEPC versus CRPC (n = 73) patient samples. Illustrated genes are bivalent and bound by N-Myc in LNCaP-N-Myc cells without androgen at D4. **(D)** Fold change expression of the indicated genes based on qRT-PCR data (n = 3 technical replicates) in PM154 following EZH2 knockdown (see Western Blot inset). *** p < 0.001, Sidak-Bonferroni adjusted two-tailed t-test.